THE ROBOTICS INSTITUTE, CARNEGIE MELLON UNIVERSITY

Pittsburgh, PA 15213

Towards Geometric Motion Planning for 3-link Kinematic Systems

CMU-RI-TR-20-44

Submitted in partial fulfillment of the requirements for the degree of Master of Science in Robotics

Thesis Committee

Prof. Howie CHOSET

Dr. Matthew TRAVERS

Prof. Ross HATTON

Julian WHITMAN

Shuoqi CHEN

July 2020

Summary

Geometric mechanics offers a powerful mathematical framework for studying locomotion for mobile systems. Despite the well-established literature, challenges still remain when using geometric mechanics to design gaits for robots made of multi-link chain, and in this thesis, we will look at two of them. First, for a large class of nonholonomic systems, singular configurations appear when constraints are violated, resulting in infinite quantities in the equations of motion that govern the motion of the robot. Second, most geometric mechanics models rely heavily on system symmetry in $SE(2)$ (i.e. invariance of system dynamics and constraints with respect to the system orientation) to simplify motion analysis. As a result, locomotion is rarely studied on non-flat surfaces which break the symmetry assumption.

In this work, we take initial steps in establishing a formal understanding of those two fundamentally different challenges under a common framework of three-link kinematic system. The thesis is organized in two parts. The first part focuses on addressing the effect of singularities when designing gaits for a 3-link kinematic snake in SE(2). We show how to combine our singularity treatment with an adapted variational optimizer to find high-efficiency gait under the defined cost metrics. The second part focuses on understanding the geometric properties of a novel 3-link kinematic system on curved position space, specifically on the cylindrical surface. Interesting features arise when the surface curvature imposes additional mechanical constraints on the system, thereby making the locomotion analysis, such as the local connection and total lie bracket, dependent on system orientation.

Acknowledgements

I would like to begin by expressing my deepest appreciation to my committee. I am grateful to my advisors Professor Choset and Dr. Travers, who continuously show me guidance and support over the course of those two years. Weekly meetings with Prof. Choset and Dr. Travers have always been enlightening, and I always come out with as many thought-provoking ideas as advice on how to become a better communicator. I also whole-heartedly appreciate the support from Julian Whitman, who never fails to give me motivation and insightful feedback when I need it the most. I would also like to extend my special thanks to Professor Hatton at Oregon State University, who through many discussions helps me develop a deepened understanding in mathematics. I owe a great part of this thesis to his unvarying encouragement and technical support. I certainly cannot forget my research partner Ruijie Fu. I am so very lucky to work with her on many of the topics presented in this thesis; the countless discussions we have had were always filled with knowledge and wonder.

I am grateful to everyone in the Biorobotics Lab for making me feel at home. My thanks to my best pal Ben Freed for being my friend, roommate, and mountain biking companions; to Tianyu for filling my days with laughter, and to others who I will always remember for the happy time we spent together. My special regards to, in no particular order, Shuo Yang, Lu Li, David Neiman, Jaskaran Grover, and Peggy Martin. I am so glad that I had the opportunity to work with you all.

I must add that my time at Robotics Institute at Carnegie Mellon University has taught me not only how to be a well-rounded researcher but also how to act as a caring and responsible individual. My graduate school experience would have never been complete without all the help and support. To all the people at RI, I am grateful to be a part of this big family.

Table of Contents

List of Figures v

1 Introduction 1

2 Background 3
2.1 Geometric Motion Planning 4
2.1.1 Reconstruction Equation 4
2.1.2 Connection Vector Field 4
2.1.3 Lie Bracket Techniques and the Importance of Coordinate Choice 5
2.2 Variational Gait Optimizer 5
2.2.1 Efficiency Cost Function 6
2.2.2 Gradient Components of the Optimizer 6

3 Part I: Gait Optimization with Singularity Treatment for Three-Link Kinematic Snake in SE(2) 7
3.1 System Model 8
3.2 Singular Configurations 9
3.3 Optimization for High-Efficiency Gaits 10
3.3.1 Approximating the $\nabla_p g_\Omega$ term at Singularity 11
3.3.2 Singularity Crossing Constraints 14
3.3.3 Optimizer Implementation Details 16
3.3.4 Choice of Seed Gait 16
3.4 Results and Discussion 17
3.4.1 Gait optimality 18
3.4.2 On-singularity and Off-singularity gaits 18
3.4.3 Relaxing the No-slip Constraint 19
3.5 Section Summary 21

4 Part II: Towards Motion Planning for Three-link Kinematic System on Cylindrical Surface 22
4.1 System Model . . . 23
4.1.1 System Mechanical Constraints . . . 24
4.1.2 Control and Compliant Angle Relationship . . . 26
4.1.3 Choice of System Parameters . . . 26
4.1.4 Nonholonomic Constraints . . . 27
4.1.5 Reconstruction Equation . . . 28
4.2 Lie Bracket Averaging . . . 31
4.2.1 Derivation of Local Curvature . . . 32
4.3 Section Summary . . . 36

5 Conclusion and Future Work 39

A Appendix 41
A.1 Pathlength Cost Metric . . . 41
A.2 Inertial Cost Metric . . . 43
A.3 The Geometry of System on Cylinder . . . 44
A.3.1 Calculation of ψ_i . . . 44
A.3.2 Calculation of θ_i . . . 46
A.3.3 Calculation of ϕ_i . . . 47
A.4 Average Body Frame for System on Cylinder . . . 48

Bibliography 51

List of Figures

3.1 The geometric configuration of the three-link kinematic snake robot in $SE(2)$, adapted from Ross et al[10]. Passive wheelsets on the links of the system prevent lateral slippage while freely allowing longitudinal translation. The control inputs are the joint angles, and though system body frame is shown on the middle link, it could be chosen differently 8

3.2 From left to right, kinematic snake connection vector fields and constraint curvature functions (CCFs) of the three position space components x, y and θ, all in optimized body coordinates. each CCF corresponds to a row in the system's local curvature $D(-\boldsymbol{A})$ defined in [12]. The value of the CCF at each point correspond to the local curvature at the shape space location [12]. Red regions of the CCFs are positive and black regions are negative. The singularity configuration of the system correspond to the $\alpha_1 = \alpha_2$ line in the plots above, as the singularity effect causes discontinuities in function values. 9

3.3 An example of three-link kinematic snake in singular configuration. The directions of the three constraint forces acting on the wheel set of each link intersect at a common point, meaning that one is redundant given the other two. 11

3.4 This figure illustrates the change in area caused by points immediate adjacent to the singularity line moving in directions orthogonal to the local curvature. The two points on either side of the singularity line move in pairs to respect the system nonholonomic constraints. . 13

3.5 The volume of constraint curvature function within boundary is approximately the sum of microscopic circulation, shown in the graphs above. For boundary enclosing infinitesimally narrow strip, the circulations stack up along the singularity line. 14

3.6 a) the best local minimums in terms of locomotion efficiency when using eqn[3.17] to describe the seed gait. The plot is axis symmetric around origin. Red regions corresponds to positive efficiency and black values correspond to negative efficiency. The green circles shows the best A, B values. b) the figure shows the corresponding shape space trajectory corresponding to the green circles in a). The trajectory is overlaid on connection vector field in body frame forward direction. 17

3.7 Snapshots of 3-link kinematic snake locomotion corresponding to different timesteps during the optimzied, high-efficinecy gait. The timesteps are linearly sampled over the entire gait and thus show the slower system movement when passes the singular configuration. 18

3.8 Performance comparison of selected gaits. a) gaits visualized in shape space. b) position space trajectories from executing the gaits. c) normalized efficiency of the gaits. The selected seed gaits are: i) & ii) on-singularity and off-singularity circular gaits that are often selected due to their low net rotation; iii) optimizer input gait selected via exhaustive search; and iv) optimally efficient gait from the variational optimization. 19

3.9 Optimally efficent gaits of using low Reynolds number swimmer with various drag ratio to approximate the effect of kinematic snake with relaxed "no slip" assumption. From left to right, the longitudinal-to-lateral drag ratio are 2, 10^3, and 10^8. Notice that singularity crossing constraints are not needed for the gait optimization result shown here. 20

4.1 Configuration of the three-link kinematic snake system on cylinder, which utilizes 3D joints to conform to the curvature of the locomotion surface. The system moves on the inner wall of the cylinder, and the wheelsets contact the surface with strictly enforced mechanical constraints. 23

4.2 System on cylinder fiber space setup. θ is the azimuth angle between the reference direction X on the cylinder cross-sectional plane and the line from the centerline to the projection of wheel-cylinder contact point p; Z is the direction along the centerline, and ϕ is the angle between the link and the cylinder cross-section, projected onto the tangent plane located by the p 24

4.3 Geometric relationship between control angle α and compliant angles β, γ. a) The control angles α_1, α_2 shown on the local tangent plane defined by the wheel-cylinder contact points. b) The yaw (α), pitch(β) and roll(γ) of the 3D joints, with the local frame x, y and z in $SE(3)$ defining the rotational axes. The relationship between the angles is presented in Eqn[4.1]and[4.1.2] 25

4.4 The special configuration of system on cylinder in which the ends of the distal and proximal links are the closest to, but not going through, the cylindrical surface. a) cross-sectional view of the cylinder. b) side view of the cylinder. 27

4.5 The change in connection vector field of the system on cylinder with respect to initial orientation ϕ_0. a) $\phi_0 = -\pi/2$; b) $\phi_0 = -\pi/3$; a) $\phi_0 = -\pi/4$; a) $\phi_0 = 0$. The shape space singularity line is overlaid on top of the surface plot to indicate the quiver plot change. 30

4.6 Visualization of how the local connection vector fields A_b change with respect to different system orientation ϕ_0. Red color indicates regions where connection vectors rotate counterclockwise with increasing value of ϕ_0, and black otherwise. 31

4.7 The change in the local curvature $D(-\boldsymbol{A})$, now composed of three components, with respect to system initial orientation ϕ_0. a) $\phi_0 = -\pi/2$; b) $\phi_0 = -\pi/3$; a) $\phi_0 = -\pi/4$; a) $\phi_0 = 0$. For easier visualization, the values are applied through the atan function are between $[-\pi/2, \pi/2]$. The shape space singularity line is overlaid on top of the surface plot to indicate the surface plot change. 36

4.8 This figure shows the effect of initial orientation ϕ_0 of the system on cylinder on the position space motion. a) the five shape space trajectories (gaits) have the same circular profile when projected in α_1, α_2 plane. b)three-dimensional visualization of the the shape space trajectories, starting at $\phi_0 = [-\pi/2, -\pi/4, 0, \pi/4, \pi/2]$. c) position space trajectories of each of the five gaits, indicated with their respective orientation. Depending on ϕ_0, the net displacement and rotation of those gaits are different. 37

4.9 The comparison between how initial orientation of the system affect position space locomotion in b) kinematic snake in $SE(2)$ and c) system on cylinder. The red solid lines show the position space trajectories of the respective systems in different initial orientation. All resulting trajectories are from the same gait shown in a). 38

A.1 Variables needed for calculating the geometric relationship between link orientation and the yaw, pitch roll angles via trigonometry . . . 45

A.2 Simple sketch showing one of the feasible mechanical design for the 3D joint, composed of three one-dimensional rotational joint controlling yaw(α), pitch(β), roll(γ) individually 45
A.3 Intermediate variables need to calculate projection of link i from $SE(3)$ to the local tangent plane defined the ith wheel-cylinder contact point 46

Chapter 1

Introduction

Many biologically-inspired robots composed of multi-link chain utilize undulatory motion to move through challenging terrains. We view those robots as having internal degrees of freedom which, when controlled strategically, result in desired displacement. Those internal shape changes, when periodic, are called gaits, and the geometric mechanics provides theoretic foundation to analyze and select good gaits. Understanding how the internal shape change of these systems transfer to useful body motions has led to many important insights on robot designs that mimic biological organisms.

Despite the rich body of literature, challenges still remain when employing geometric mechanics tools to design desirable gaits for the link-like robots. First of all, for a large class of link-like systems with nonholonomic constraints, singular configurations appear when nonholonomic constraints are violated (e.g. one or more of the constraint equations becomes a linear combination of the others), at which point infinite qualities occur in the equations of motion. The singularity poses challenges to the use of many classical geometric tools, and thus is often simply avoided without much exploration. Secondly, current research in geometric mechanics models relies heavily on system symmetry $SE(2)$ (i.e. invariance of system dynamics and constraints with respect to coordinate choice) to simplify motion analysis. As a result, locomotion is rarely studied on non-flat surfaces that break the symmetry assumption, which is usually what robots will encounter in the real world environment. In this thesis, we take first steps in establishing formal understanding of those two challenges and develop corresponding solutions to them.

In the grander scheme of geometric mechanics, the singularity problem and the symmetry-breaking problem evolve around fundamentally separate topics, with the former appearing primarily in nonholonomic kinematic snake models and the latter extending to a much broader spectrum of mobile systems. Because of this, we divide our work in this thesis into two disjointed parts. Nevertheless, due to the scope of our study, we connect our approaches and intermediate solutions of those problems

through the common framework of three-link kinematic nonholonomic systems. In the first part, we show that rather than avoiding singularity, gait designs for kinematic snake in $SE(2)$ that purposefully enclose the singularity region can produce high efficient gaits. In the second part, we present a new mechanical model of the 3-link nonholonomic kinematic system that works with a cylindrical surface. We show that, through derivation of the reconstruction equation and total Lie brackets of the new system, the effect of surface curvature towards locomotion manifest through an dependency on body coordinate orientation.

Chapter 2

Background

Much of the geometric locomotion framework for the multi-chain systems can be traced back to Walsh and Sastry [1], who pioneered the work of planar three-link systems. They derived a specific form of the Lagrangian to generate gaits for snake-like robots. Ostrowski and Burdick et al. [2] took advantage of the idea of translational symmetry from physics and projected the entire dynamics of the system onto the joint space; this relates system control inputs and the corresponding body position changes. Additionally, they combined the reconstruction equation with Lie bracket theory to generate sinusoidal gaits. Using this approach, they intuitively developed and analyzed gaits for kinematic systems with nonholonomic constraints. Shammas et al [3] and other researchers [4] combined the idea of Stokes' theorem with the reconstruction equation to define "height functions" - the curl of the connection vector field - on the shape space of the three-link robots. This opened up opportunities to design visual tools to select desirable system locomotion patterns. Hatton and Choset [5] addressed the limitation of the "height functions" that makes them only useful when designing small cyclical gaits. They introduced a choice of coordinates that reduced the approximation error by making appropriate choices of system parameterization. More recently, Ramasamy and Hatton [6, 7] developed a gradient-based optimizer for drag-dominated systems. The cost metric used in the optimizer, which measures locomotion efficiency, is in line with Hatton's work on kinematic cartography and uses curvature of system constraints for the power dissipation metric[8]. By using the gradient-based optimizer, Faraji et al.[9] developed a framework for motion planning in inertia-dominated systems. A new inertial cost metric is designed to better account for the energy dissipated through the robots actuators.

Building on top of the aforementioned theoretical foundation, in this thesis we focus on establishing geometric understanding of locomotion for the three-link kinematic systems, both in $SE(2)$ and on the surface of a cylinder. Hence, we provide a brief overview of geometric mechanics concepts that are essential to

analyzing and designing gaits, such as the reconstruction equation and the Lie bracket technique. Having established the mathematical preliminaries, we will also look at recent developments in gait optimization using a variational optimizer. Specifically, we discuss the gradient components of the developed optimizer and the efficiency metric used for performance evaluation.

2.1 Geometric Motion Planning

2.1.1 Reconstruction Equation

For mobile systems, the configuration space Q is naturally composed of the position space G and shape space M, such that the position $g \in G$ locates the system in the world, and the shape $r \in M$ tells the relative arrangements of each component of the system. $Q = M \times G$ is a trivial principal fiber bundle, where M is the base space, and G is the fiber space [3]. When describing the system locomotion in body coordinates, the body representations of the robot dynamics and constraints formulate a connection on configuration space Q, which describes allowable combinations of body and shape velocities to locomote.

The geometric mechanics community has exploited this connection structure with the development of the kinematic reconstruction equation[1, 2, 3]. For principally kinematic systems, where the holonomic constraints are invariant to the system position and orientation, the kinematic reconstruction equation takes the following form:

$$\mathring{g} = -\boldsymbol{A}(r)\dot{r} \tag{2.1}$$

where $\mathring{g}$ represents the system body frame velocities. and the local connection $\boldsymbol{A}(r)$ maps the system shape velocities $\dot{r}$ to those body velocities. The biggest advantage of formulating the kinematic reconstruction equation is that it reduces control of the whole system to control of the system's shape.

2.1.2 Connection Vector Field

In the reconstruction equation, the local connection $\boldsymbol{A}(r)$ acts as a Jacobian-like matrix linking shape velocity and position velocity, thus capturing the relationship between shape and position changes. Hatton and Choset[10] further expanded the geometric meaning of $\boldsymbol{A}(r)$ and created connection vector fields, which can be used to identify the translation and rotation components of a shape space trajectory. Mathematically, the connection vector field are the covectors in the ith row of $-\boldsymbol{A}(r)$, where the ith component of the system position space velocity is $\boldsymbol{A}^i(r)$.

$$\mathring{g}_i = \boldsymbol{A}^i(r) \cdot \dot{r} \tag{2.2}$$

where the superscript i is the ith row of the local connection $-\boldsymbol{A}(r)$. By representing the local connection as sets of vector fields on the shape space, motion planners can more easily identify useful shape changes that generate forward, lateral or rotational system motion.

2.1.3 Lie Bracket Techniques and the Importance of Coordinate Choice

Lie-bracket theory has long be identified as a useful tool to design gaits for mobile systems. Ostrowski and Burdick[4, 11] combined the reconstruction equation with Lie bracket and Stokes' theorem to generate sinusoidal gaits that translate and rotate a variety of snakelike systems. However, only gaits with very small amplitude in the shape space can be considered as a infinitesimal oscillation of the shape, so the Lie bracket was only used to explain net motion resulting from small cyclical shape inputs. Explaining the motion of a large amplitude gait was challenging because, in their work, the approximation accuracy of the translational motion depends on different choices of body coordinates.

In Hatton and Choset[12], they separated out the non-conservative and the noncommuntative components from the Lie bracket derivation. They showed that with appropriate choice of body coordinate, the non-communtative effect can be diminished and thus geometric integration via Stoke's theorem gives good approximation of the system true displacement over big-amplitude gaits. The optimal choices of such body coordinate, called the minimum perturbation coordinate, minimizes the rotation of the body frame in response to changes in system shape. We refer the readers to [12, 13] for detailed information.

2.2 Variational Gait Optimizer

Using Lie brackets of the system dynamics can help engineers to empirically select gaits that that yield large net forward displacement. However, two obstacles hinder more versatile gait designs. First, the noncommutativity in the equations of motion means that Lie brackets averaging provides only an approximation of the displacement induced by a gait, and the error increases with the amplitude of the shape input. Second, the traditional "hand-drawn" gaits are not guaranteed to be anywhere near the optimal solution under sophisticated evaluation metrics.

To mitigate these problems, Ramasamy and Hatton[7] developed a variational optimizer which encodes the previously developed geometric insights into a gradient-descent solver. In their work, analytical expressions are replaced by numerical search along a potentially high-dimensional space of gait parameters, thereby speeding up the gait design process and resulting in gaits with improved performance. For

the sake of completion, the next two subsections provide a brief summary of cost function as well as the optimization gradients. We refer the readers to [7, 6] for a comprehensive discussion of optimizer design details.

2.2.1 Efficiency Cost Function

When considering locomoting robots, it is often useful to observe the efficiency of locomotion such that the energy expended to produce a given displacement is minimized. The the efficiency of locomotion can thus be calculated by dividing the net displacement of the gait by the cost to execute the gait:

$$\eta = \frac{g_\Omega}{s} \tag{2.3}$$

We assign g_Ω to be the net displacement over the gait, and cost s to be the system effort to compete the gait. For locomotion system with inertial effect, Hatton et al. [9] devised an alternative cost s_T, which is a function of combined torque exerted by the system joint motors to execute a specific gait in unit time T

$$s_T = \left(\int_0^1 \tau^2 \right)^{1/4} \tag{2.4}$$

The equivalent cost function s_T constrains the total gait execution time and this makes the system to move as fast as it can while operating under finite power. Therefore, $\eta = \frac{g_\Omega}{s_T}$ is used as the efficiency cost function of the optimizer.

2.2.2 Gradient Components of the Optimizer

The gradient of the locomotion efficiency η with respect to a gait parametrization p can be written as:

$$\nabla_p \eta = \nabla_p \frac{g_\Omega}{s_T} = \frac{1}{s_T} \nabla_p g_\Omega - \frac{g_\Omega}{s_T^2} \nabla_p s_T \tag{2.5}$$

The differential equation in Eqn[2.5] shows an analogy to the formation of a soap bubble: the first term, which contains $\nabla_p g_\Omega$, seeks to expand the gait trajectory in order to achieve more gait displacement, and the second term, which contains $\nabla_p s$, seeks to constrain the growth of the bubble [7]. To search for the maximally-efficient gait, we perform gradient descent on Eqn[2.5]. The locally optimal result is found when the gradient of the local efficiency $\nabla_p \eta$ equals to 0:

Chapter 3

Part I: Gait Optimization with Singularity Treatment for Three-Link Kinematic Snake in SE(2)

The three-link nonholonomic kinematic system, or the kinematic snake robot, is a multi-body locomotion system. Each link of kinematic snake can only move in its longitudinal direction but not the lateral direction due to the presence of passive wheels. Those constraints on link-wise velocity are called nonholonomic constraints, and they dictates the motion of the kinematic snake to be purely governed by its shapes changes. Cyclical shape changes, called gaits, are developed to produce useful system body motion, and choosing appropriate gaits are important to improve the locomotion performance of the kinematic snake robot.

One of the challenges in designing desirable gaits for the kinematic snake is that the system can enter singular configurations, or singularity. Mathematically, the local connection matrix becomes rank-deficient at singularity and its inverse is analytically unsolvable. The singularity poses challenges to the use of many geometric motion planning tools and thus is often deliberately avoided. In this work, we propose a new singularity treatment method that numerically approximates the effect of the singularity on the system locomotion. We implemented our method within an adapted framework of a variational gait optimizer to find the locally optimally efficient gait for the three-link kinematic snake. We show that, rather than avoiding singularity, gait designs that purposely enclose the singularity region can ultimately produce the best results given specified cost functions.

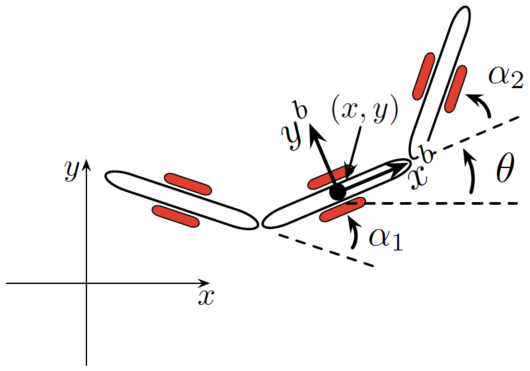

Figure 3.1: The geometric configuration of the three-link kinematic snake robot in $SE(2)$, adapted from Ross et al[10]. Passive wheelsets on the links of the system prevent lateral slippage while freely allowing longitudinal translation. The control inputs are the joint angles, and though system body frame is shown on the middle link, it could be chosen differently

3.1 System Model

The framework of the three-link, nonholonomic kinematic snake is presented in [3]. Here, we briefly discuss key concepts and equations for completeness. The configuration of the kinematic snake denoted by $q = (g, r) \in Q = G \times M$, where Q is the configuration composed by position space G and shape space M. Fig.3.1 shows an example of the kinematic snake model. The position and orientation of the system is denoted as $g = (x, y, \theta) \in G = SE(2)$ and is placed at the center of the middle link. The shape of the system is parametrized by the two joint angles, $r = (\alpha_1, \alpha_2)$. The separation of position space G and shape space R is beneficial: the position $g \in G$ locates the system in the world, and the shape $r \in M$ gives the relative arrangements of its bodies.

For kinematic snake, the wheels at the centers of the links create a set of nonholonomic constraints that confine the system's motion. The constraints can be written in the form

$$\begin{bmatrix} 0 \\ 0 \\ 0 \end{bmatrix} = \begin{bmatrix} \dot{x} \\ \dot{y} \\ \dot{\theta} \end{bmatrix} = A(q) \begin{bmatrix} \dot{\alpha}_1 \\ \dot{\alpha}_2 \end{bmatrix} \tag{3.1}$$

Normalized for unit body-length, the reconstruction equation for kinematic

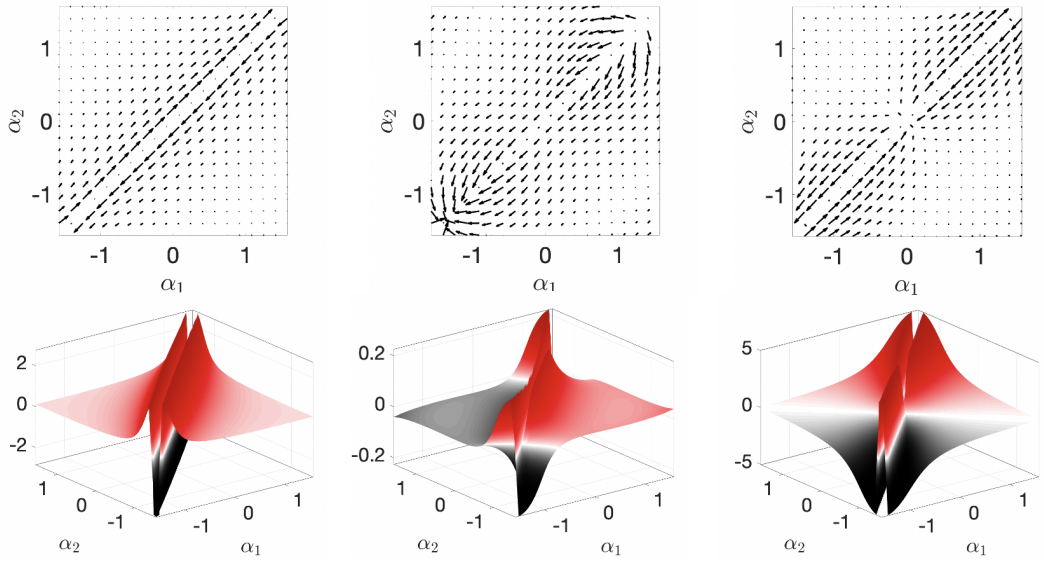

Figure 3.2: From left to right, kinematic snake connection vector fields and constraint curvature functions (CCFs) of the three position space components x, y and θ, all in optimized body coordinates. each CCF corresponds to a row in the system's local curvature $D(-\boldsymbol{A})$ defined in [12]. The value of the CCF at each point correspond to the local curvature at the shape space location [12]. Red regions of the CCFs are positive and black regions are negative. The singularity configuration of the system correspond to the $\alpha_1 = \alpha_2$ line in the plots above, as the singularity effect causes discontinuities in function values.

snake can be explicitly written as the following:

$$\begin{bmatrix} \mathring{g}_x \\ \mathring{g}_y \\ \mathring{g}_\theta \end{bmatrix} = -\frac{1}{D} \begin{bmatrix} (1+\cos\alpha_2)/6 & (1+\cos\alpha_1)/6 \\ 0 & 0 \\ \sin\alpha_2 & \sin\alpha_1 \end{bmatrix} \begin{bmatrix} \dot{\alpha}_1 \\ \dot{\alpha}_2 \end{bmatrix} \tag{3.2}$$

where $D = \sin\alpha_1 - \sin\alpha_2 + \sin(\alpha_1 - \alpha_2)$

3.2 Singular Configurations

In mechanical systems, singular configurations are those where the required body velocities and other physical quantities become infinite due to the loss of a degree

of control freedom. Motion planning for those mechanical systems usually stays away from such configurations to avoid infinite operation cost[14]. For the nonholonomic kinematic snake robot, singular configurations appear when the mapping between joint and system body frame velocity becomes rank insufficient, resulting in discontinuities in calculations. This corresponds to situations where $\alpha_1 = \alpha_2$ An example of the singularity configuration of the kinematic snake is shown in Fig(3.3). Geometrically, the directions of the three constraint forces all intersect at a common point, meaning that one constraint is redundant given the other two [15]. When this happens, the local connection matrix becomes singular. However, it is possible for the system to transition through the singular configuration while respecting the nonholonomic constraint. Plugging $\alpha_1 = \alpha_2$ into Eqn[3.2] yields a shape velocities constraint such that $\dot{\alpha_1} = -\dot{\alpha_2}$. When representing the shape space as a 2D space spanned by α_1 and α_2, the system will need to go across the $\alpha_1 = \alpha_2$ line at a right angle.

The idea of smoothly guiding the two joint velocities $\dot{\alpha_1}$ and $\dot{\alpha_2}$ to be equal and opposite as the system approaches singularity has been briefly explored in [15, 14]. Tony Dear devised a hybrid kinodynamic model that pulls the system into zero joint velocities for singularity crossing, which allow the system to exhibit transient dynamic properties. However, this kinodynamic method requires joints to be locked ($\dot{\alpha_1} = -\dot{\alpha_2} = 0$) at singular configuration and that the system requires external forcing to exit the dynamic mode.

In our work, we assume singularity crossing is transient, and thus joint locking is not required as long as $\dot{\alpha_1} = -\dot{\alpha_2}$. Our assumption corresponds to the physical intuition that an instantaneous "drift" happens to the kinematic snake when one control input becomes compliant while the whole system velocity is non-zero. Moreover, the system continues to behave kinematically after this instantaneous drift. Because singularity treatment is often specific to the chosen motion planning strategy, our analysis of system locomotion at the singularity is presented with combination of the gait-optimization framework recapped below.

3.3 Optimization for High-Efficiency Gaits

The gradient-descent based gait optimizer has the benefit of automatically converging to local optimal results that are challenging to discover by traditional methods. The efficiency cost of the optimizer is represented as net gait displacement g_Ω divided by gait execution cost T For a gait parametrization p, the maximum efficiency occurs when gradient of efficiency $\frac{g_\Omega}{T}$ becomes zero as in Eqn[2.5].

An important design factor of the optimizer is gait parametrization. In order to easily derive the gait displacement and cost as well as their gradients with respect to the gait parametrization variables, we use two parallel methods, first

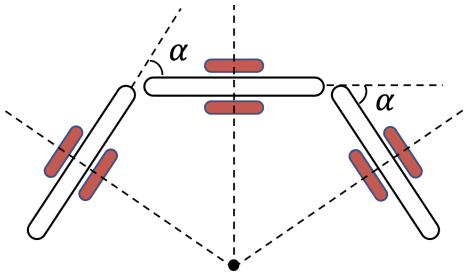

Figure 3.3: An example of three-link kinematic snake in singular configuration. The directions of the three constraint forces acting on the wheel set of each link intersect at a common point, meaning that one is redundant given the other two.

developed by Ramasamy and Hatton [7], to describe the shape of the gait. The first method is called the direct waypoint parametrization, which assign points to shape space trajectory equally spaced in time. The second method is called the Fourier parametrization, which uses low-dimensional Fourier series to capture the gait's cyclical nature. The synergy of the two parallel gait parametrizations is crucial. Whereas the direct way points provide convenient, discrete method to calculate the surface integral, the Fourier functions make it possible to impose constraints necessary to preserve the system's kinematic properties at the singularity configuration.

In Eqn[2.5], we have written the gradient of gait efficiency in two components, which together bear similarity to the growth of the soap bubble. In terms of numerical calculation, the $\nabla_p s$ term can be calculated by finding the partial derivatives of the cost with respect to the gait parametrization. Derivation details of $\nabla_p s$ are discussed in [9], and are not repeated here. However, the calculation of $\nabla_p g_\Omega$ term potentially involves surface integral of singularity-enclosing area, and therefore it deserves careful treatment discussed in the next section.

3.3.1 Approximating the $\nabla_p g_\Omega$ term at Singularity

Considered independently, the gradient term $\nabla_p g_\Omega$ pushes the gait towards the shape that yields the maximal displacement. In shape space regions where the body velocity integral approximate the true system displacement well, the net displacement g_Ω of a given gait Ω is approximately the line integral of the body velocity along the gait cycle [5]. This line integral can be approximated by an area integral of total Lie Bracket $D(-\boldsymbol{A})$ of the local connection over the surface Ω_a

bounded by the cycle [12].

$$g_\Omega \approx \int_\Omega \boldsymbol{A}(r)\ dr \approx \iint_{\Omega a} D(-\boldsymbol{A})\ dr_1 dr_2 \tag{3.3}$$

To examine how variations in gait parametrization p changes the net displacement g_Ω, we calculate the gradient term $\nabla_p g_\Omega$ via an application of the Leibniz integral rule. This allows us to re-write the gradient of the area integral g_Ω in Eqn[3.3] as the interior product of the integral's boundary gradient with its integrand.

$$\nabla_p \iint_{\Omega_a} D(-\boldsymbol{A}) = \oint_\Omega (\nabla_p \Omega) \lrcorner D(-\boldsymbol{A}) \tag{3.4}$$

where $D(-\boldsymbol{A})$ is the local curvature of the connection and can be visually represented in the surface plot in Fig(3.2) [12]. The right-hand side of Eqn[3.4] can be discretely approximated by summing up the variations of gait-enclosed area induced by the waypoint movements along the gait multiplied by the corresponding $D(-\boldsymbol{A})$ values at corresponding waypoints. In terms of implementation, the variations of the gait-enclosed area induced by each waypoint is captured by a triangle formed by the waypoint to-be-moved and its two neighbors [7]. Since the value of $D(-\boldsymbol{A})$ is finite everywhere but the singularity, this discrete approximation method is applicable to all waypoints except for those at or adjacent to the shape space singularity line.

As shown in Fig.(3.2), values of $D(-\boldsymbol{A})$ go to infinity at the singularity, and therefore multiplying this unbounded $D(-\boldsymbol{A})$ to a finite quantity will produce an infinite value. To tackle this problem, we introduce a new method to infer the infinite values while properly preserving the effect of singularity to the system. Instead of calculating $D(-\boldsymbol{A})$ directly at singularity, we numerically approximate this value from discrete waypoints immediately adjacent to the singularity. To do this, we find the four closest points near singularity, two on each side of the singularity line. We define two local directions: $e_\parallel = p_i - p_{i-1}$ and $e_\perp \perp e_\parallel$, as shown Fig.(3.4), where p_i and p_{i+1} form a pair of waypoints which immediately neighbor the singularity line from both side. Closely following the method in [7], this pair of waypoints is moved together in the $e_\perp$ direction to ensure the line segment $p_i - p_{i-1}$ crosses the singularity line perpendicularly. Movements of those points induce a change in the waypoint-enclosed area, which we will refer to as the "generalized chevron".

As before, the optimization gradient component $\nabla_p g_\Omega$ at the pair of waypoints p_i and p_{i-1} can be calculated by multiplying the change in waypoint-enclosed area by the corresponding $D(-\boldsymbol{A})$ values. Whereas the $D(-\boldsymbol{A})$ value corresponding to the two triangular regions on either side of the generalized chevron are finite and can be used directly, the $D(-\boldsymbol{A})$ value corresponding to rectangular region in the middle sits directly at singularity and needs to be treated specially. Special treatment has

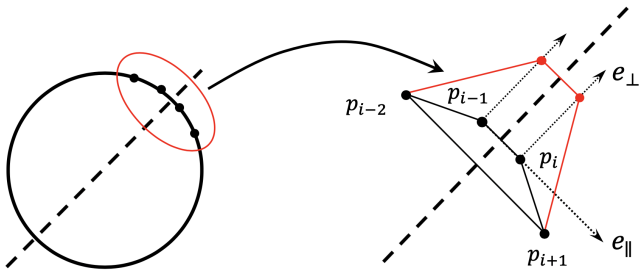

Figure 3.4: This figure illustrates the change in area caused by points immediate adjacent to the singularity line moving in directions orthogonal to the local curvature. The two points on either side of the singularity line move in pairs to respect the system nonholonomic constraints.

to take place at singularity because, ideally, the waypoints p_i and p_{i-1} are infinitely close to each other to accurately represent the shape of the gait. In that case, the segment $p_i - p_{i-1}$ produces 0 length and so is the area of the rectangle region. Therefore, simply multiplying the 0-area of the rectangle to an infinite $D(-\boldsymbol{A})$ value gives an indeterminate answer. However, we can numerically approximate the indeterminate answer by a two-step method; first we approximate the $D(-\boldsymbol{A})$ by the curl of the system connection vector field[12], and then we approximate the curl using a microscopic circulation. Referring back to the definition of the Green's Theorem, the sum of all the differentially small circulation that is inside the closed boundary equates the macroscopic circulation around the boundary:

$$\int_{\Omega} A(r) = \iint_{\Omega_a} \text{curl } A(r) \cdot \hat{n} \tag{3.5}$$

Since the co-vectors $A_x(r)$ of the kinematic snake are equal and opposite on either side of the singularity line (and no vector component goes perpendicularly across singularity) a microscopic circulation sitting across singularity line can be represented as:

$$\text{microscopic circulation} \approx A^x_{p_i}(r) - A^x_{p_j}(r) \tag{3.6}$$

In this way, the effect of surface integral of an infinitely slim region around the singularity, can be represented as adding up those "microscopic circulation" along $e_\perp$. Consequently, the internal pressure associated with the rectangular region can be calculated as:

$$\nabla_p \phi_{\text{rectangle}} = \frac{1}{N} \sum_{k=1}^{N} A^x_{p_i^k}(r) - A^x_{p_j^k}(r) \tag{3.7}$$

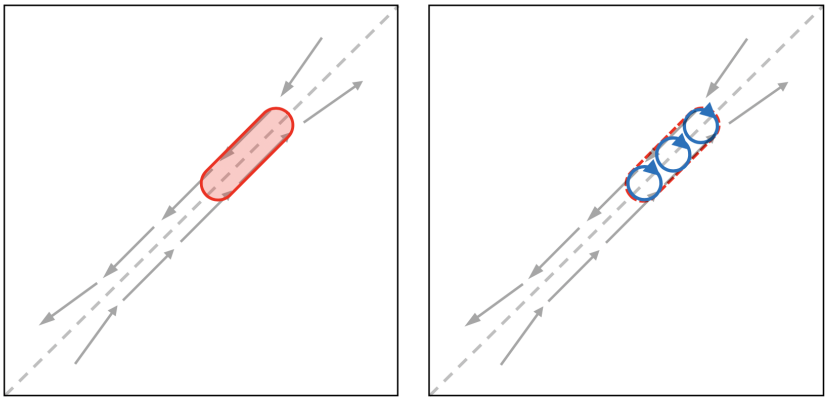

Figure 3.5: The volume of constraint curvature function within boundary is approximately the sum of microscopic circulation, shown in the graphs above. For boundary enclosing infinitesimally narrow strip, the circulations stack up along the singularity line.

where k is the number of query points sampled along $e_\perp$. In implementation, the effect $\nabla_p \phi_{\text{rectangle}}$ is shared by both of the way points at either side the of singularity.

3.3.2 Singularity Crossing Constraints

As discussed in the previous section, for gaits passing through singularity and at the same time respecting nonholonomic constraints, the trajectory curvature in shape space has to cross the singularity line at a right angle. This is equivalent to maintaining joint angular velocities of $\dot{\alpha_1} = -\dot{\alpha_2}$, which forms a special velocity constraint on the system. Any other pair of joint velocities that are not equal and opposite will violate the wheel set "no slip" condition at the singular configurations. It is therefore important for gait parametrization methods to incorporate this velocity constraint to model the locomotion of kinematic snake correctly.

In our implementation, the optimization gradient is applied to the Fourier transcription of the gait, which is composed of two low-order Fourier functions which individually describes each of the joint angles. The gait can be represented as follows:

$$\Omega(t) = \begin{bmatrix} \alpha_1(t) \\ \alpha_2(t) \end{bmatrix} = \begin{bmatrix} \sum_{j=1}^{k} \left[a_j^{\alpha_1} \cos(i\omega t) + b_j^{\alpha_1} \sin(i\omega t) \right] + c^{\alpha_1}] \\ \sum_{j=1}^{k} \left[a_j^{\alpha_2} \cos(i\omega t) + b_j^{\alpha_2} \sin(i\omega t) \right] + c^{\alpha_2}] \end{bmatrix} \tag{3.8}$$

a_i^α, b_i^α, and c^α are Fourier coefficients, and k is the order of the Fourier functions. The presence of Fourier frequency $\omega = 2\pi$ guarantees that the gait is closed and that the shape formed by the first Fourier components loops around exactly one time give a time period of $T = 1$. We can arrange those gaits such that they pass through singularity at $t_1 = 1/2$ and $t_2 = 1$. Correspondingly, we impose the "crossing singularity line at right angle" constraint such as shape velocity at t_1, t_2 is orthogonal to the direction of the singularity line.

$$\frac{d\alpha_1(t)}{dt}|_{(t_1,\ t_2)} = -\frac{d\alpha_2(t)}{dt}|_{(t_1,\ t_2)} \tag{3.9}$$

Using the Fourier parametrization of the gait, Eqn[3.9] yields:

$$\sum_{i=1}^{k} \left(a_j^{\alpha_1} j\omega \sin(j\omega t) + b_j^{\alpha_1} j\omega \cos(j\omega t) + \ a_j^{\alpha_2} j\omega \sin(j\omega t) + b_j^{\alpha_2} j\omega \cos(j\omega t)\right) |_{(t_1,\ t_2)} = 0 \tag{3.10}$$

With $t_1 = 1/2$ and $t_2 = 1$, and plug in $\omega = 2\pi$, the equation can be further simplifed as:

$$\sum_{j=1}^{k} \omega j \left(b_j^{\alpha_1} + b_j^{\alpha_2}\right) = 0 \tag{3.11}$$

Eqn[3.11] is valid when the gait passes through singularity exactly at $t_1 = 1/2$ and $t_2 = 1$. To ensure this happens, we impose a second constraint on joint angles such that:

$$\alpha_1(t)|_{(t_1,\ t_2)} = \alpha_2(t)|_{(t_1,\ t_2)} \tag{3.12}$$

Parametrize $\alpha_1(t),\ \alpha_2(t)$using fourier functions, we have

$$\sum_{j=1}^{k} \left[\left(a_j^{\alpha_1} \cos(j\omega t) + b_j^{\alpha_1} \sin(j\omega t)\right) - \left(a_j^{\alpha_2} \cos(i\omega t) + b_j^{\alpha_2} \sin(i\omega t)\right)\right] |_{(t_1,\ t_2)} + c^{\alpha_1} - c^{\alpha_2} = 0 \tag{3.13}$$

*

With the same conditions $t_1 = 1/2$ and $t_2 = 1$, $\omega = 2\pi$, we arrive at:

$$\sum_{j=1}^{k} \left(a_j^{\alpha_1} - a_j^{\alpha_2}\right) + c^{\alpha_1} - c^{\alpha_2} = 0 \tag{3.14}$$

3.3.3 Optimizer Implementation Details

3.3.4 Choice of Seed Gait

The aforementioned optimizer uses Body Velocity Integral (BVI) as an approximation of system displacement over gait. BVI is a reliable measurement of displacement over a gait if the system rotation during the execution is small at all time [5]. This is given by the error ϵ_ζ between the BVI and displacement over an arbitrary gait:

$$\epsilon_\zeta = \int_\Omega \begin{bmatrix} 1-\cos\theta & \sin\theta & 0 \\ -\sin\theta & 1-\cos\theta & 0 \\ 0 & 0 & 0 \end{bmatrix} \begin{bmatrix} \mathring{g}_x \\ \mathring{g}_y \\ \mathring{g}_\theta \end{bmatrix} \tag{3.15}$$

Since BVI and the later developed corrected body velocity integral (cBVI) are building blocks of height-function-based visual gait designs, identifying situations where ϵ_ζ is small is instrumental to discover desirable gaits that produces forward displacement as expected [12]. The optimizer operates in regions with large rotations will not only generate incorrect optimization gradient, but also risk being trapped in undesirable local minimum.

To ensure that the gait optimization process converges to the desired optimum, we carefully choose initial shape space trajectory input, called seed gait, from the best-performing seed gaits obtained from an exhaustive search in a low-dimensional Fourier parametrization space. Since the lowest frequency sinusoidal waves of Fourier functions are dominant and largely determines the size and the shape of the composed gait, we can simplify Eqn[3.8] to arrive at the form:

$$\Omega'(t) = \begin{bmatrix} \alpha_1(t) \\ \alpha_2(t) \end{bmatrix} = \begin{bmatrix} c^{\alpha_1} + a_1^{\alpha_1}\cos(\omega t) + b_1^{\alpha_1}\sin(\omega t) \\ c^{\alpha_2} + a_1^{\alpha_2}\cos(\omega t) + b_1^{\alpha_2}\sin(\omega t) \end{bmatrix} \tag{3.16}$$

In addition, We are interested in gaits with small net rotations, both to reduce ϵ_ζ and to encourage large forward motion with respect to the system's body frame. To this end, we focus on the behaviour of symmetrical gaits that are centered in shape space, which leads to simplified parametrization.

$$\Omega'(t) = \begin{bmatrix} \alpha_1(t) \\ \alpha_2(t) \end{bmatrix} = \begin{bmatrix} a_1\cos(\omega t) + b_1\sin(\omega t) \\ a_1\cos(\omega t) + b_1\sin(\omega t) \end{bmatrix} \tag{3.17}$$

The Fourier functions above generate elliptical gaits with various principal axis lengths and align with the singularity line. The simplified parametrization has the additional benefit of easy visualization. With only two free variables a and b, we can identify regions with high displacement, and subsequently, gait efficiency directly on plot shown in Fig(3.6).

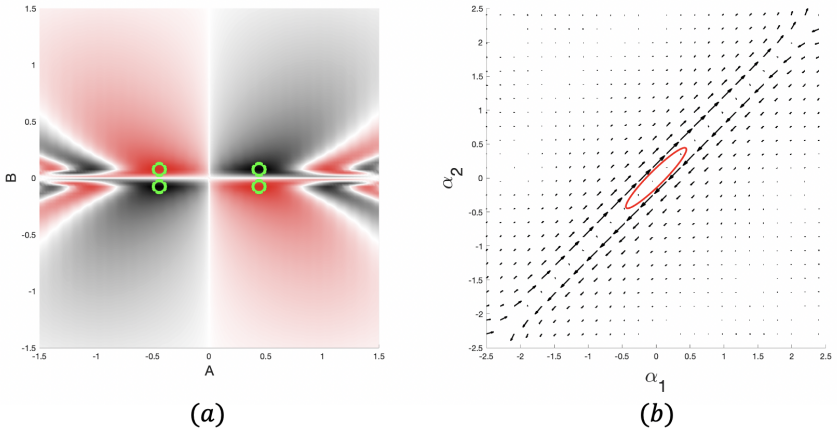

Figure 3.6: a) the best local minimums in terms of locomotion efficiency when using eqn[3.17] to describe the seed gait. The plot is axis symmetric around origin. Red regions corresponds to positive efficiency and black values correspond to negative efficiency. The green circles shows the best A, B values. b) the figure shows the corresponding shape space trajectory corresponding to the green circles in a). The trajectory is overlaid on connection vector field in body frame forward direction.

Notice that multiple efficiency optimums appear near the singularity configuration, but only some optimums lie in the region where ϵ_ζ is small. Since the best efficiency optimums are fortunately associated with small ϵ_ζ, we choose them to form the seed gait for our optimization process.

3.4 Results and Discussion

Fig.(3.7) shows the final result of the optimized gait for forward-moving motion of the nonholonomic kinematic snake. Notice that two longer sides of the the optimal gait track very close to the singularity line $[\alpha_1 = \alpha_2]$. The narrow shape gives high forward displacement because it encompasses much negative sign-definite volume on the x constrained curvature function. Moreover, the optimized gait has two important shape characteristics: 1) it cross singularity in almost a straight-line. 2) it has rounded corner before and after crossing singularity. Both of the characteristics help avoid large joint velocity changes and corresponding reduce the inertial cost.

Comparing to the previously hand-selected gaits that avoid singular configuration, the optimal gait found by the developed optimizer is intuitively advantageous in both forward travel and cost of transport. Our result also has very little net rotation over gait cycle, which we expect due to its symmetry about the shape

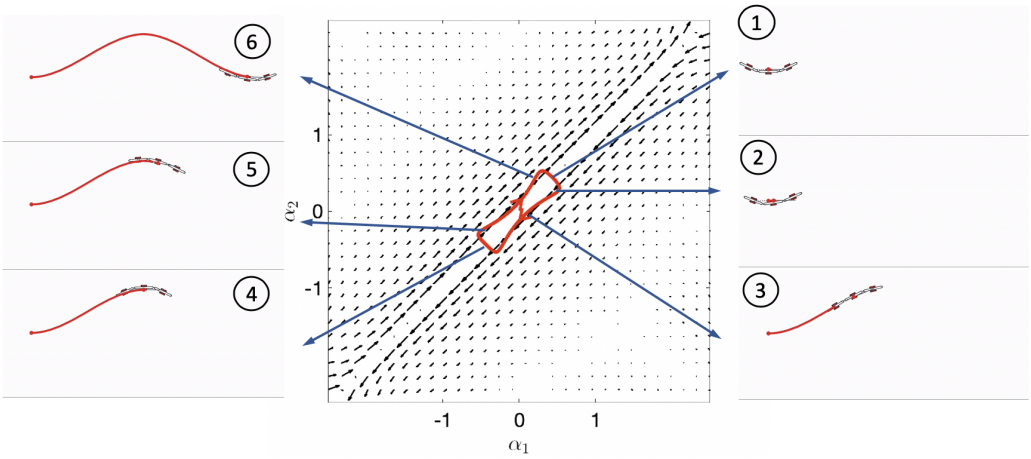

Figure 3.7: Snapshots of 3-link kinematic snake locomotion corresponding to different timesteps during the optimzied, high-efficinecy gait. The timesteps are linearly sampled over the entire gait and thus show the slower system movement when passes the singular configuration.

space origin, resulting in zero or minimum net volume on the θ component of constrained curvature function.

3.4.1 Gait optimality

While the proposed method yields a high-efficiency gait for kinematic snake, it is possible that the result is a local optimum, as the gradient-descent based optimizer does not guarantee convergence to global optimum. Additionally, since we parametrize the gait using low-order Fourier functions, which has limited expressiveness, gaits with more complicated shape could possibly produce even higher displacement-to-cost ratio. In general, however, it is up to the designer to decide what specific goals to achieve and criteria to satisfy. Our group is interested in optimal gaits that are of high efficiency, self-intersection free, and have zero or low net rotation over each gait cycle. The resulting gait therefore represents the best result that meets our specifications.

3.4.2 On-singularity and Off-singularity gaits

Although gaits that follow very closely to the singular configuration benefit from large forward displacement, they also suffer from rather relatively large inertial cost. In contrast, gaits that are centered far away singularity have lower inertial cost, due to their smaller fiber space velocity change per shape space velocity

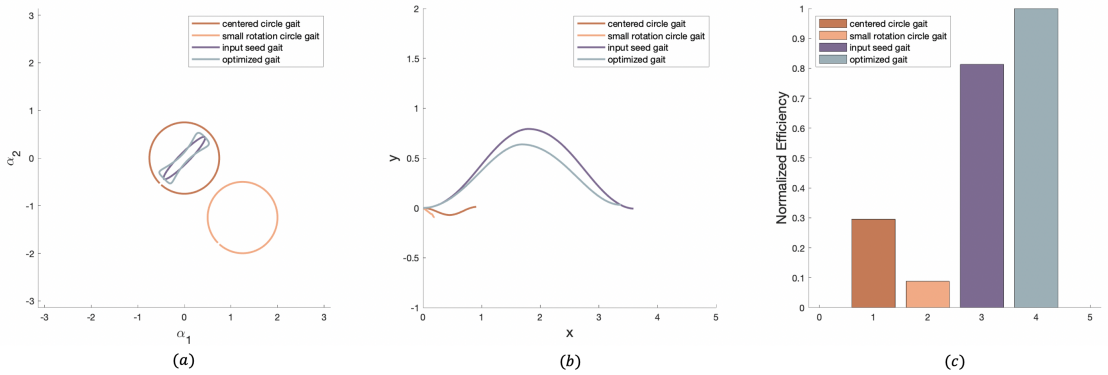

Figure 3.8: Performance comparison of selected gaits. a) gaits visualized in shape space. b) position space trajectories from executing the gaits. c) normalized efficiency of the gaits. The selected seed gaits are: i) & ii) on-singularity and off-singularity circular gaits that are often selected due to their low net rotation; iii) optimizer input gait selected via exhaustive search; and iv) optimally efficient gait from the variational optimization.

change when away from singularity configuration. Potentially, the reduced inertial cost can also lead to high efficiency, even when the gait displacement is low (e.g. the system moves forward in small but easy "wiggles").

To examine the possibility that additional local optimum of gait efficiency would appear in gaits centered away from singularity, we perform experiments on selected circular seed gait on $\alpha_1 = -\alpha_2$ line. The particular choice of seed gait location is to include zero or minimum rotation over gait cycle, and hopefully set the start of the optimization process close to its local optimum.

From Fig.(3.8), we can observe the off-singularity gait has lower efficiency, and the displacement performance is poorer than that of the on-singularity optimal gait. Moreover, the sub-optimal gait gives rise to the "cusp" - quick zig-zag motion that shows up in sharp turning in the fiber space trajectories. The "cusp" appears when the gait aligns with zero magnitude forward-direction connection vector field and large magnitude rotational connection vector field, and are rather undesirable in application as it diverts motion and energy in counter-productive directions.

3.4.3 Relaxing the No-slip Constraint

Until now, we have proposed and implemented an optimization strategy that centers around handling the singularity of kinematic snake. Nevertheless, in real life, locomotion systems such as the n-link snake robot will often slip as it passes singular configuration. The slippage could happen when the ground surface provides insufficient traction. To examine how slippage would affect the gait optimization,

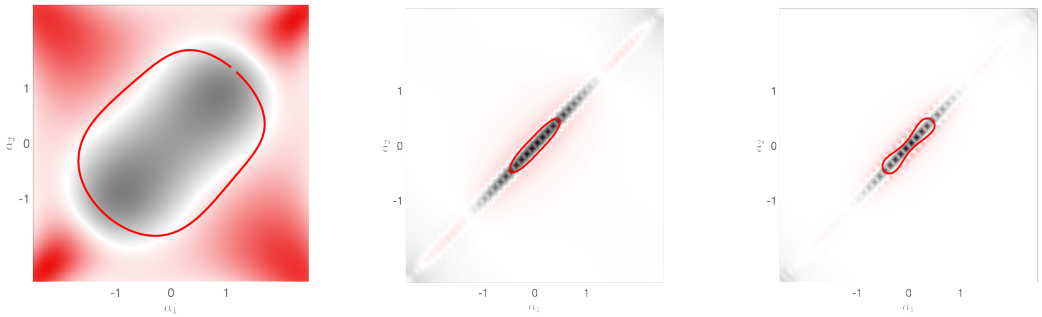

Figure 3.9: Optimally efficent gaits of using low Reynolds number swimmer with various drag ratio to approximate the effect of kinematic snake with relaxed "no slip" assumption. From left to right, the longitudinal-to-lateral drag ratio are 2, 10^3, and 10^8. Notice that singularity crossing constraints are not needed for the gait optimization result shown here.

we relax the kinematic snake "no-slip" assumption and approximate its system locomotion using an adapted low Reynolds (quasistatic) system model.

While it seems that locomotion of nonholonomic kinematic snake is governed by geometric constraints and thus different from that of the low Reynolds swimming systems, there are in fact strong underlying similarities. Previous literature has shown that, with two small changes, low Reynolds number swimmer can be converted into the three-link kinematic snake [13]. First, concentrating the lateral force at the link centers and assign zero rotational moment to the force acting points simulates the ground forces acting on the wheels. Second, adjusting the lateral-to-longitudinal drag ratio to ∞ approximates the "no-slip" condition on the wheels of the nonholonomic kinematic snake. Overall, two systems resemble each other at the limit due to the similar composition of their system Pfaffian constraints: both multiplying the body and shape velocities to produce a zero vector. We can thereby exploiting this similarity and approximate the slipping behavior of an otherwise nonholonomic system by varying the lateral-to-longitudinald drag ratios of a quasistatic swimmer. This correspond to a kinematic snake with wheels that will give away to strong external force, much the same as what would happen in the physical world.

Fig.(3.9) shows the result of applying the same optimization procedure to the aforementioned, adapted low Reynolds number system. We can see that as the drag ratio increases, the gait optimization result for three-link low Reynold number swimmer becomes more similar to that of the kinematic snake. However, the approximated optimal gait is rounder at the ends, suggesting that violating the now non-existent nonholonomic constraint may not incur as big a cost penalty.

3.5 Section Summary

In this work, We incorporated tools from geometric mechanics into the developed gradient-descent solver and created special procedures to capture the effect of singularity for the 2D nonholonomic kinematic snake. We summarized the singularity crossing condition as the equal and opposite movement of the input joint right before and after reaching the singular configurations, and we implemented this condition in tune with our Fourier gait parametrization. Furthermore, we adapted the variational gradient descent optimizer to find the high-efficiency gait for the kinematic snake. Our results show that high-efficiency gaits for kinematics snake tracks close to the singular configuration for higher displacement and forms a straight line when crossing singularity for lower cost. We also examined the effect of relaxing "no-slip" assumption and showed the evolution of the optimal results with respect to varying degrees of this relaxation.

Looking forward, we plan to further our singularity treatment for the kinematic systems to work with general motion planning methods. For example, future work has been planned to develop more expressive gait parametrizations, such as piecewise linear spline, in order to fine-tune the shape of optimal gaits. Making our singularity treatment adaptable to different gait design tools will lay a strong foundation for future research.

Chapter 4

Part II: Towards Motion Planning for Three-link Kinematic System on Cylindrical Surface

The kinematic snake robot is a canonical example of a principally kinematic system, one whose motion is governed by nonholonomic constraints[1, 2]. Much of the mathematical elegance of the three-link kinematic snake arise from its inherent symmetry, which correspond to the fact that the system dynamics and constraints are invariant to changes in the system's position or orientation in space. Therefore, we can express the system velocity in body coordinates instead of inertial coordinates. Early work by Kelly and Murray[16] established the reconstruction equation for the nonholonomic systems, which relates body velocity to changes in internal shape. Hatton and Choset later formulated the concept of the body-velocity integral (BVI) and identified coordinate choices that minimizes the body frame rotation in response to shape changes[13].

The use of system symmetry means that most studies of kinematic snake models are dedicated to locomotion in $SE(2)$ without any external actuation. However, real-world robots often move on non-flat terrains or are under the influence of directional forces; thus there is a lack of gait design frameworks for symmetry-breaking systems. Recently, Dear took a step towards part of the problem by introducing the stratified fiber function, which split the original local connection into internal and external components[17]. Nevertheless, the strategy was tailored to the kinematic snake moving under external actuation and is difficult to extend to other cases. In this work, we take a different approach and examine how curvature

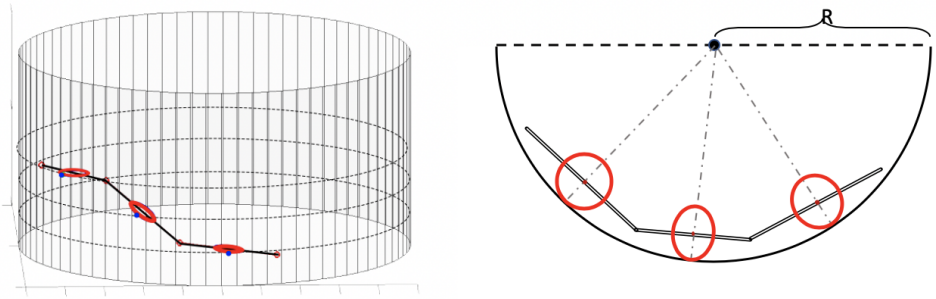

Figure 4.1: Configuration of the three-link kinematic snake system on cylinder, which utilizes 3D joints to conform to the curvature of the locomotion surface. The system moves on the inner wall of the cylinder, and the wheelsets contact the surface with strictly enforced mechanical constraints.

of the locomotion surface (or parametrized position space) breaks symmetry. To do so, we study a newly designed three-link kinematic system model on cylinder. This new model allows us to explore to what extent the traditional geometric concepts, such as the local connection and the lie bracket techniques, can be used in motion planning on curved position space. Utilizing visualization tools commonly employed by the geometric mechanics community, we show the relationship between system motion and its body frame orientation. Furthermore, we build upon the gradient-descent gait optimizer and present a complete strategy to optimize a gait for the system on cylinder.

4.1 System Model

To study the effect of position space curvature on a locomotion system, one intuition is to add in directional curvature along a single coordinate basis component. For example, if we take a 2D plane and bend the x axis with constant curvature, we will effectively create a cylindrical surface. Mobile systems that realistically locomote on such surfaces are met with new concerns. Not only do they need to overcome gravity, but they also need to have mechanical structures which conform to the curvature. In situations where gravity can be ignored (i.e. the elevation loss/gain is negligible), a system still needs to ensure locomotion is collision-free. It is thus useful to create a well-defined system that addresses the aforementioned concerns. To this end, we create what we refer to as the system on cylinder, a kinematic model designed to constrain its motion on cylindrical surfaces yet simple enough

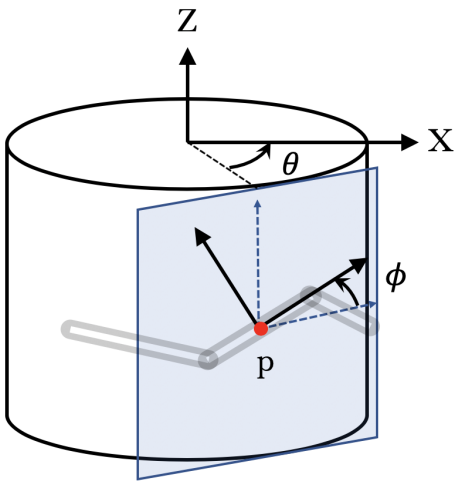

Figure 4.2: System on cylinder fiber space setup. θ is the azimuth angle between the reference direction X on the cylinder cross-sectional plane and the line from the centerline to the projection of wheel-cylinder contact point p; Z is the direction along the centerline, and ϕ is the angle between the link and the cylinder cross-section, projected onto the tangent plane located by the p

for generalized geometric mechanics analysis.

4.1.1 System Mechanical Constraints

Similar to the kinematic snake robot, the proposed system on a cylinder consists of three rigid links, each of unit length and with wheelsets located at the link center. The wheels contact the inner wall of the cylinder and can roll forward but are forbidden to slip sideways. The links in the system are connected by 3D joints which have full yaw (α), pitch(β) and roll(γ) degrees of freedom.

Using cylindrical coordinates, each contact point between the wheel and the cylindrical surface defines a local tangent plane with position $[\theta,\ R,\ z]$. Furthermore, we specify the orientation of the link by the angle ϕ between the link itself and the cross-section of the cylinder, projected onto the local tangent plane. For a cylindrical surface with a constant radius R, the position and orientation of each link i can be uniquely defined by the set of position variables $[\theta_i,\ z_i,\ \phi_i]$. We thus define the θ_o, z_o, positions and ϕ_o orientation of the middle link of the system as its position variables. Correspondingly, we define the system body frame to be located at the center of the middle link and whose orientation ϕ_o is in the tangential plane

To succinctly describe the system configurations, we impose two important mechanical constraints such that:

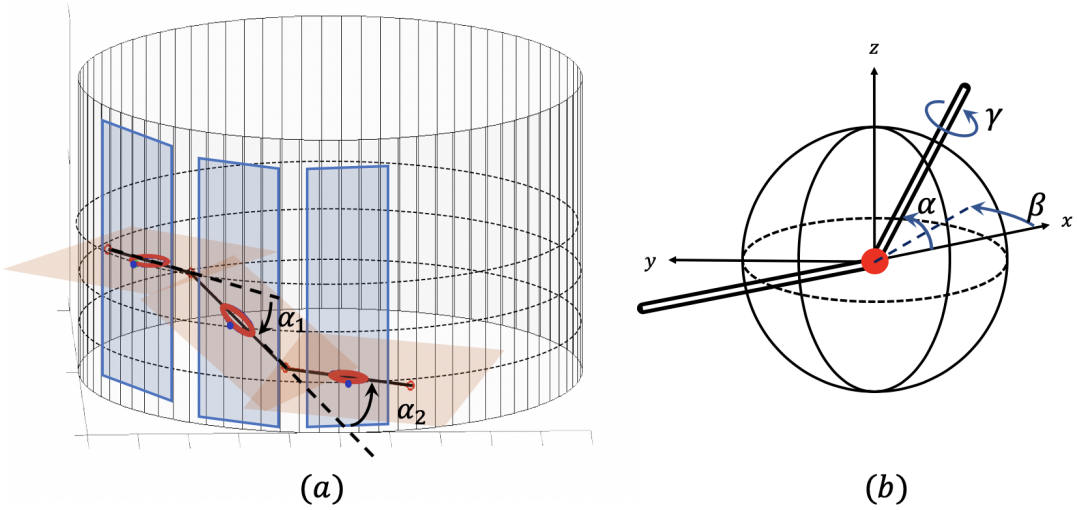

Figure 4.3: Geometric relationship between control angle α and compliant angles β, γ. a) The control angles α_1, α_2 shown on the local tangent plane defined by the wheel-cylinder contact points. b) The yaw (α), pitch(β) and roll(γ) of the 3D joints, with the local frame x, y and z in $SE(3)$ defining the rotational axes. The relationship between the angles is presented in Eqn[4.1]and[4.1.2]

- Constraint 1: Each wheel has one and only one contact point with the inward cylindrical surface at all time, and the discs of the wheels are perpendicular to the local tangent planes of the cylinder at the contact points.

- Constraint 2: Both ends of the middle link have the same distance to the cylinder center line, preventing it from tilting.

Constraint 1 essentially specifies how the 3D joints can controlled. We propose one feasible mechanical scheme of the 3D joint, shown in Appendix A, to utilize the reduced joint angle space. Suppose each 3D joint is composed by a serial chain of three rotation joints that controls the yaw (α), pitch(β), roll(γ) Euler angles in sequence. When one of the three joint angles is being actively controlled, the other two become functions of the active joint angle and the middle link orientation ϕ_o in order to satisfy constraint 1. In the following section, we choose the two yaw angles $[\alpha_1,\ \alpha_2]$ as our control inputs. that pitch and yaw angle pairs are calculated accordingly to in order satisfy constraint 1. Accordingly, we call $[\alpha_1,\ \alpha_2]$ as our shape variables as they describe the links relative positions of the links.

4.1.2 Control and Compliant Angle Relationship

The relationship between the compliant angles $[\beta, \gamma]$, and the control angle α and orientation variable ϕ_o are purely geometric and can be represented in the following equations.

$$(2(R\ -\ r)+l\sin\beta)^2\ +l^2\ (\cos\phi_o+\ \cos\beta\cos(\alpha-\phi_o))^2\ -4(R\ -\ r)^2=\ 0 \tag{4.1}$$

$$\begin{aligned} l(\sin(\phi_o+\alpha)\cos\gamma-\cos(\alpha+\phi_o)\sin\beta\sin\gamma)(\cos\phi_o+cos(\phi_o+\alpha)\cos\beta)+\cdots \\ \cos\beta\sin\gamma(2r-2R+l\sin\beta)=0 \end{aligned} \tag{4.2}$$

Where R is the cylinder radius and r is the wheel radius. The two equations above calculate the α and β angles for the distal link (i.e. link $i+1$) in the system but can be adapted for the proximal link (i.e. link $i-1$) without the loss of generality. Additionally, even though the above equations are for the system moving on inward surface of the cylinder, the relationship between α, β, γ and ϕ_o can be generalized to systems moving on the outward cylindrical surface with a just few swaps of signs the equations above.

The complexity of Eqn[4.1]and Eqn[4.1.2] makes it hard to obtain analytical solutions whenever β and γ are involved. For this reason, we choose to represent many of the variables in the following sections in their partial derivatives forms and solve the values from a numerical approach.

4.1.3 Choice of System Parameters

The aforementioned mechanical constraints as well as the control/compliant angle relationships allow us to establish a complete kinematic model of the system. The system configuration space can be written as $Q = M \times G$, where $g = (\theta_o, z_o, \phi_o)^T \in G$ encodes the position and the orientation of the middle link in the inertial frame. The active joint angles $r = (\alpha_1, \alpha_2) \in M$ determines the shape of the system by specifying the links' relative orientations.

Since the system geometry determines its kinematics, we provide the specific values we choose for some of the geometric parameters. We set the links to be unit length such that $l = 1 and the wheel radius$r=0.2.

In the real world, the cylinder radius R is a given parameter by the environment. But physically, there is a minimal R for every system on cylinder below which the links would penetrate the cylinder wall at certain configurations. In fact, if R satisfies:

$$R \geqslant \frac{l^2}{4r} + \frac{r}{2} \tag{4.3}$$

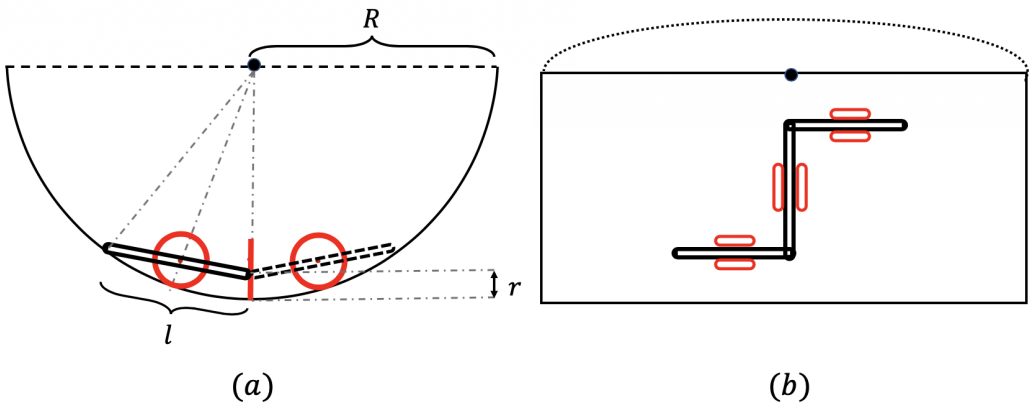

Figure 4.4: The special configuration of system on cylinder in which the ends of the distal and proximal links are the closest to, but not going through, the cylindrical surface. a) cross-sectional view of the cylinder. b) side view of the cylinder.

then the system is collision-free, given it meets the two constraints in the previous section. To study how the effect of the curvature of cylindrical surface affects the system locomotion to its extreme, we choose $R = 1.35$, which is the smallest cylinder radius that is allowed.

4.1.4 Nonholonomic Constraints

The proposed system on a cylinder has passive wheelsets on the links, which prevent lateral translation while freely allowing rotation and longitudinal translation. Those constraints on link-wise velocity, called nonholonomic constraints, determine the allowable combination of inertial frame position and shape velocity and can be written as the following

$$\begin{aligned} -R\dot{\theta}_l \sin\phi_l + \dot{z}_l \cos\theta_l &= 0 \\ -R\dot{\theta}_o \sin\phi_o + \dot{z}_o \cos\theta_o &= 0 \\ -R\dot{\theta}_r \sin\phi_r + \dot{z}_r \cos\theta_r &= 0 \end{aligned} \tag{4.4}$$

where $R\dot{\theta}_i$ is the linear velocity tangential to the curvature at the wheel-cylinder contact point p_i. Given the system geometry, we can formulate relationships between link-wise position and orientation and the control angles α_1, α_2. Detailed derivations of those relationships, as well as the solution of intermediate variables, are provided in Appendix A.

The linkwise position velocity $\dot{\theta}_i$, written in inertial frame, can be represented as:

$$\dot{\theta}_i = \frac{\partial}{\partial t}\theta_i \ (\theta_o, \phi_o, \alpha_i) = \ \frac{\partial \theta_i}{\partial \theta_o}\dot{\theta}_o + \frac{\partial \theta_i}{\partial \phi_o}\dot{\phi}_o + \frac{\partial \theta_i}{\partial \alpha_i}\dot{\alpha}_i \tag{4.5}$$

Multiplying the cylinder radius to get the tangential linear velocity $x_i = R\dot{\theta}_i$ at link i

$$\dot{x}_i = R\left(\frac{\partial \theta_i}{\partial \theta_o}\dot{\theta}_o + \frac{\partial \theta_l}{\partial \phi_o}\dot{\phi}_o + \frac{\partial \theta_l}{\partial \alpha_l}\dot{\alpha}_i\right) = \left(\frac{\partial \theta_i}{\partial \theta_o}\left(R\dot{\theta}_o\right) + \left(R\frac{\partial \theta_i}{\partial \phi_o}\right)\dot{\phi}_o + \left(R\frac{\partial \theta_i}{\partial \alpha_i}\right)\dot{\alpha}_i\right) \tag{4.6}$$

The same process can be repeated for calculating total differential of z_i, which is a function of $z_o,\ \phi_o$ and α_i.

$$\dot{z}_i = \frac{\partial}{\partial t}z_i = \frac{\partial z_i}{\partial z_o}\dot{z}_o \ + \frac{\partial z_i}{\partial \phi_o}\dot{\phi}_o + \frac{\partial z_i}{\partial \alpha_i}\dot{\alpha}_i \tag{4.7}$$

Substitute expressions in Eqn[4.5] and [4.1.4] into Eqn[4.1.4], we arrive at the equation of the form:

$$-\sin\phi_l\left(\dot{x_o} + \frac{\partial x_l}{\partial \phi_o}\dot{\phi}_o \ + \frac{\partial x_l}{\partial \alpha_l}\dot{\alpha}_l\right) + \ \cos\phi_l\left(\dot{z_o} + \frac{\partial z_l}{\partial \phi_o}\dot{\phi}_o + \frac{\partial z_l}{\partial \alpha_l}\dot{\alpha}_l\right) \ = \ 0$$

$$-\sin\phi_o\ (\dot{x}_o) + \ \cos\phi_o(\dot{z}_o) \ = \ 0$$

$$-\sin\phi_r\left(\dot{x_o} \ + \frac{\partial x_r}{\partial \phi_o}\dot{\phi}_o \ + \frac{\partial x_r}{\partial \alpha_r}\dot{\alpha}_r\right) \ + \ \dot{z}_r\cos\phi_r\left(\dot{z_o} \ + \frac{\partial z_r}{\partial \phi_o}\dot{\phi}_o + \frac{\partial z_r}{\partial \alpha_r}\dot{\alpha}_r \ \right) \ = \ 0 \tag{4.8}$$

4.1.5 Reconstruction Equation

Reforming the nonholonomic constraints in Eqn[4.1.4] in linear form yields:

$$\overbrace{\begin{bmatrix} -\sin\phi_l & \cos\phi_l & -\sin\phi_l\cdot\frac{\partial x_l}{\partial \phi_o} + \cos\phi_l\cdot\frac{\partial z_l}{\partial \phi_o} \\ -\sin\phi_o & \cos\phi_o & 0 \\ -\sin\phi_r & \cos\phi_r & -\sin\phi_r\cdot\frac{\partial x_r}{\partial \phi_o} + \cos\phi_r\cdot\frac{\partial z_r}{\partial \phi_o} \end{bmatrix}}^{\omega(\mathring{g})} \begin{bmatrix} \dot{x_o} \\ \dot{z_o} \\ \dot{\phi_o} \end{bmatrix} + \ldots$$

$$\overbrace{\begin{bmatrix} -\sin\phi_l\cdot\frac{\partial x_l}{\partial \alpha_l} + \cos\phi_l\cdot\frac{\partial z_l}{\partial \alpha_l} & 0 \\ 0 & 0 \\ 0 & -\sin\phi_r\cdot\frac{\partial x_r}{\partial \alpha_r} + \cos\phi_r\cdot\frac{\partial z_r}{\partial \alpha_r} \end{bmatrix}}^{\omega(r)} \begin{bmatrix} \dot{\alpha_l} \\ \dot{\alpha_r} \end{bmatrix} = \begin{bmatrix} 0 \\ 0 \\ 0 \end{bmatrix} \tag{4.9}$$

Moving the matrix sub-blocks $\omega(\mathring{g})$ and $\omega(r)$ to the same side, we have

$$\dot{g} = \ \omega(\mathring{g})^{-1}\omega(r) \tag{4.10}$$

We construct such matrix $A_{w_{(g,r)}}$ such that $\dot{g} = -A_{w_{(g,\ r)}}\dot{r}$; the minus sign is there to be consistent with the notation used in the literature.

The tangent plane defined by the middle-link contact point is locally $SE(2)$. Therefore, the mapping that takes inertial (world frame) velocity to body velocity is given by

$$T_g L_{g^{-1}} = \begin{bmatrix} \cos\phi_o & \sin\phi_o & 0 \\ -\sin\phi & \cos\phi_o & 0 \\ 0 & 0 & 1 \end{bmatrix} \tag{4.11}$$

And so,

$$\overbrace{\begin{bmatrix} \mathring{g}_u \\ \mathring{g}_v \\ \mathring{g}_\theta \end{bmatrix}}^{\mathring{g}} = \overbrace{\begin{bmatrix} \cos\theta_o & \sin\theta_o & 0 \\ -\sin\theta_o & \cos\theta_o & 0 \\ 0 & 0 & 1 \end{bmatrix}}^{T_g L_{g^{-1}}} \overbrace{\begin{bmatrix} \dot{x} \\ \dot{z} \\ \dot{\phi} \end{bmatrix}}^{\dot{g}} = \underbrace{T_g L_{g^{-1}} A_{w_{(g,r)}}}_{A_{b_{(g,r)}}} \begin{bmatrix} \dot{\alpha_1} \\ \dot{\alpha_2} \end{bmatrix} \tag{4.12}$$

$$\mathring{g} = -A_{b_{(g,r)}}\dot{r} \tag{4.13}$$

In terms of notation, we will use $\dot{g} = \begin{bmatrix} \dot{x} & \dot{z} & \dot{\phi} \end{bmatrix}^T$ to represent the inertial frame position space velocity, and $\mathring{g} = \begin{bmatrix} \mathring{g}_x & \mathring{g}_z & \mathring{g}_\phi \end{bmatrix}^T$ to represent the body frame position space velocity written in exponential coordinates. Notice that we replaced the position space parameter θ with $x = R\theta$ which give cleaner equation forms without the loss of generality.

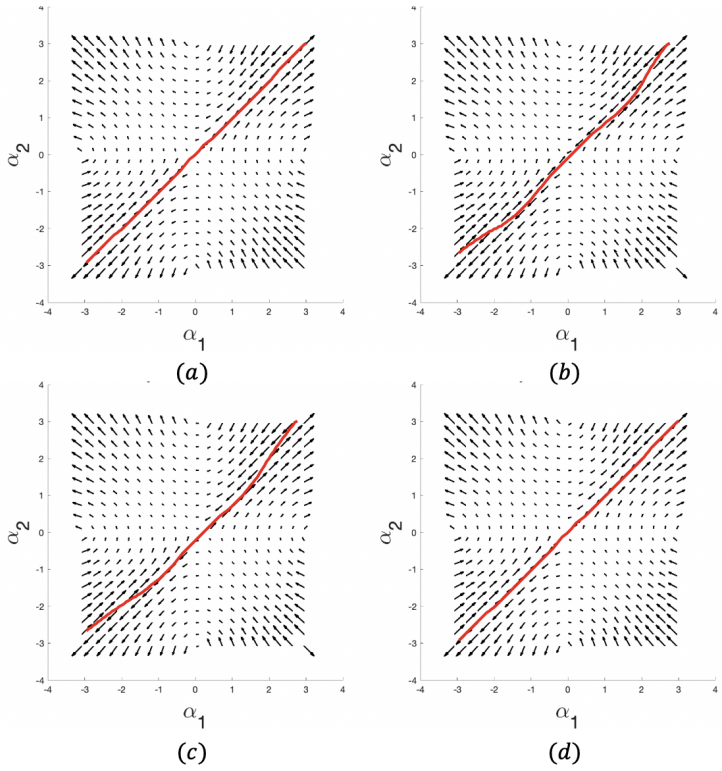

Figure 4.5: The change in connection vector field of the system on cylinder with respect to initial orientation ϕ_0. a) $\phi_0 = -\pi/2$; b) $\phi_0 = -\pi/3$; a) $\phi_0 = -\pi/4$; a) $\phi_0 = 0$. The shape space singularity line is overlaid on top of the surface plot to indicate the quiver plot change.

Eqn[4.13] above is known as the reconstruction equation, with $-A_b$ being the local form of the kinematic connection and serves as a Jacobian-like matrix that relate a system's internal shape to its external body positions. In the section below, we will be drop the dependency of the matrices on the shape and position variables, so that $A_{w_{(g,r)}}$ will be A_w and $A_{b_{(g,r)}}$ will be A_b

Notice that, different from the three-link kinematic snake in $SE(2)$, the connection A_b which maps system shape velocity to body frame velocity acquires an extra dependency on the body frame orientation ϕ_o. From the derivation above, it is clear that the dependency on ϕ_o originates in the derivation of the nonholonomic constraints, and so it implicitly reflects how curvature change in different direction of the cylinder surface affects allowable system motion.

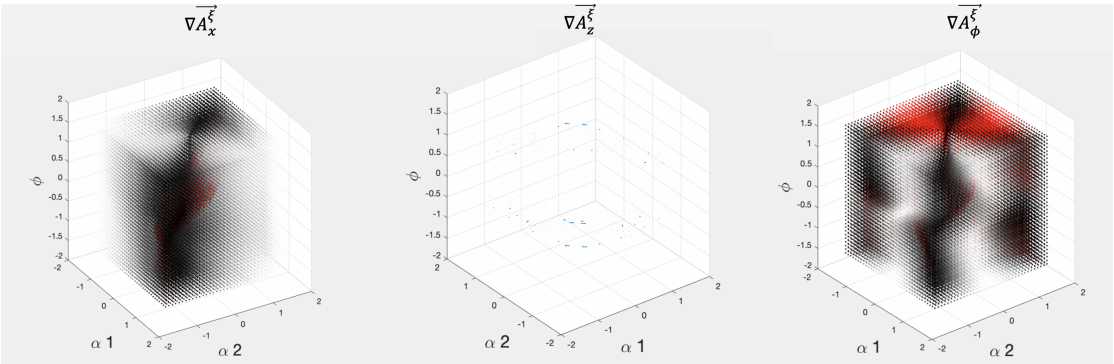

Figure 4.6: Visualization of how the local connection vector fields A_b change with respect to different system orientation ϕ_0. Red color indicates regions where connection vectors rotate counterclockwise with increasing value of ϕ_0, and black otherwise.

4.2 Lie Bracket Averaging

In their work, Hatton and Choset developed in-depth analysis on Lie bracket techniques that explores how the system constraints vary over shape and position space components[12]. The core principal of their work is that the net displacement of a gait can be approximated - although the accuracy of the approximation depends on the choice of the system body frame - by a surface integral of the constraint curvature $D(-A)$ of the local connection.

$$g_\Omega = \oint_\Omega -T_e L_g A_b \, dr \approx \iint_{\Omega_a} D(-A_b) \tag{4.14}$$

Where $D(-A)$ is also referred to as the total lie bracket, and the integral

$$\zeta = \iint_{\Omega_a} D(-A_b) \tag{4.15}$$

is formally named as the corrected body velocity integral ($cBVI$) and used frequently in averaging locomotion literature[12]. For the sake of completion, we briefly recap the formulation of Lie bracket and the constraint curvature $D(-A)$ as a result of Lie bracketing on the system full configuration space. However, readers are encouraged to review [12] for detailed derivation.

The Lie bracket of two vector fields X and Y is also a vector field defined as:

$$[X,\ Y] = (\nabla Y \cdot X) - (\nabla X \cdot Y) \tag{4.16}$$

or component-wise as:

$$[X,\ Y]^i = \sum \left(x^j \frac{\partial y^i}{\partial u^j} - y^j \frac{\partial x^i}{u^j} \right) \tag{4.17}$$

In $se(2)$, which is the Lie algebra of $SE(2)$, the lie bracket of two vectors x and y shows the effect of making infinitesimal moves in $x,\ y,\ -x,\ -y$ in sequence. On a planar surface for example, this captures the "parallel parking" effect, where a rigid body draws infinitesimal parallelograms and use oscillating translation and rotation to produce net translation in an orthogonal direction.

Similarly, a gait with very small amplitude in the shape space of the system can be considered as a infinitesimal oscillation, and the resulting motion is captured by the use of Lie brackets. For a specified input shape velocity $\dot{r}$, the system on cylinder at configuration $q\ =\ (r,\ g)$ has position velocity $\dot{g} =\ T_e L_g A_b\ \dot{r}$ within the local tangent plane. Moving with velocity $\dot{r}$ can be interpreted as flowing along the vector field $X\ (q)$ defined over the full configuration space

$$X(q) =\ \dot{q} = \begin{bmatrix} \dot{r} \\ \dot{g} \end{bmatrix} \tag{4.18}$$

If we define two unit-magnitude input shape velocities $\dot{r_1}\ = [\dot{\alpha_{l1}},\ \dot{\alpha_{r1}}]^T\ = [1,\ 0]^T$ and $\dot{r_2} = [\dot{\alpha_{l2}},\ \dot{\alpha_{r2}}]^T = [0,\ 1]^T$ then the following Lie bracket gives the average velocity vector achieved by infinitesimally flowing along the vector fields, evaluated at the initial configuration $q_0\ =\ (r_0,\ g_0)$

$$[\dot{q_1},\ \dot{q_2}] = \left[\begin{pmatrix} \dot{r}_1 \\ \dot{g}_1 \end{pmatrix}, \begin{pmatrix} \dot{r}_2 \\ \dot{g}_2 \end{pmatrix} \right] = \left[\begin{pmatrix} \frac{\partial \dot{r_2}}{\partial r}\dot{r_1} - \frac{\partial \dot{r_1}}{\partial r}\dot{r_2} \end{pmatrix} + \begin{pmatrix} \frac{\partial \dot{r_2}}{\partial g}\dot{g}_1 - \frac{\partial \dot{r_1}}{\partial g}\dot{g}_2 \end{pmatrix} \right] \Bigg|_{(q_0)} \tag{4.19}$$

$$\begin{pmatrix} \frac{\partial \dot{g_2}}{\partial r}\dot{r_1} - \frac{\partial \dot{g_1}}{\partial r}\dot{r_2} \end{pmatrix} + \begin{pmatrix} \frac{\partial \dot{g_2}}{\partial g}\dot{g}_1 - \frac{\partial \dot{g_1}}{\partial g}\dot{g}_2 \end{pmatrix}$$

The following derivation shows how we separate out and identify three of the major components of the local curvature $D(-\{A_b)$. We show that, rather than consisting of only the exterior derivative dA and the local lie bracket $[A_1,\ A_2]$, which is the case for three-link kinematic snake in $SE(2)$, for system on cylinder a third term shows up due to the orientation-dependent local connection $A_b(r,\ g)$.

4.2.1 Derivation of Local Curvature

Because we define the the input shape velocities $\dot{r_1}$ *and* $\dot{r_2}$ are constant fields, their partial derivatives with respect to the both the shape and position fields are zero.

$$\frac{\partial \dot{r_i}}{\partial r}\ =\ \mathbf{0},\ \ \frac{\partial \dot{r_i}}{\partial g}\ =\ \mathbf{0} \tag{4.20}$$

$$\left(\frac{\partial \dot{r_2}}{\partial r}\dot{r_1} - \frac{\partial \dot{r_1}}{\partial r}\dot{r_2}\right) + \left(\frac{\partial \dot{r_2}}{\partial g}\dot{g_1} - \frac{\partial \dot{r_1}}{\partial g}\dot{g_2}\right) = \mathbf{0} \tag{4.21}$$

In constrast, the partial derivtives of the position velocity fields with respect to the shape fields take more complex forms. To simplify notation, we use $\boldsymbol{A}$ to represent the local connection A_b for simplification. Using the product rule, we have:

$$-\frac{\partial \dot{g_i}}{\partial r}\Big|_{(r0,\ g0)} = \frac{\partial\ (T_e L_g \boldsymbol{A}_i)}{\partial r} = \left(\frac{\partial\ (T_e L_g)}{\partial r}\Big|_{(\ g0)} \boldsymbol{A}_{i(r0,\ g0)}\right) + \left(T_e L_{g0}\ \frac{\partial \boldsymbol{A}_i}{\partial r}\Big|_{(r0,\ g0)}\right)$$

Since $T_e L_g$ is independent of shape r

$$-\frac{\partial \dot{g_i}}{\partial r}\Big|_{(g0)} = T_e L_{g0}\ \frac{\partial \boldsymbol{A}_i}{\partial r}\Big|_{(\ (r0,\ g0))} \tag{4.22}$$

Furthermore, since we have chosen $\dot{r_1} = [1,0]^T$ and $\dot{r_2} = [0,1]^T$

$$-\frac{\partial \dot{g_i}}{\partial r}\ \dot{r_j}\Big|_{(r0,\ g0)} = T_e L_{g0}\ \frac{\partial \boldsymbol{A}_i}{\partial r_j}\Big|_{(r0,\ g0)} \tag{4.23}$$

For system in $SE(2)$, the system nonholonomic constraints are invariant to the orientation of the defined body frame and thus the system constraints are independent to the choice of coordinates. As a result, the local connection A_b also becomes invariant to the choice of coordinates, which simplifies geometric analysis. But because the curvature of the cylinder surface creates inherent relationship between position space velocity and middle link orientation, the local connection A_b becomes a function of position space variable ϕ_o. This affects the result of the total lie bracket. whereas in $SE(2)$, the partial derivatives of the position velocity fields with respect to the shape fields goes to 0, on cylindrical surface the derivatives are not. We explore the difference through the following derivation.

$$-\frac{\partial \dot{g_i}}{\partial g}\Big|_{(r0,\ g0)} = \frac{\partial\ (T_e L_g \boldsymbol{A}_i)}{\partial g} = \left(\frac{\partial T_e L_g}{\partial g}\Big|_{(\ g0)} \boldsymbol{A}_{i(r0,\ g0)}\right) + \left(T_e L_{g0}\ \frac{\partial \boldsymbol{A}_i}{\partial g}\Big|_{(r0,\ g0)}\right) \tag{4.24}$$

Using the relationship: $\dot{g_i} = T_e L_g\,(-\boldsymbol{A}\cdot\dot{r_i}) = -T_e L_g \boldsymbol{A}_i$

$$-\frac{\partial \dot{g_i}}{\partial g}\ \dot{g_j}\Big|_{(r0,\ g0)} = -T_e L_{g0}\Big(\frac{\partial (T_{g0} L_{g0-1} T_e L_g)}{\partial g}\Big|_{g0} \boldsymbol{A}_{i(r0,\ g0)} (T_e L_{g_0} \boldsymbol{A}_{j(r0,\ g0)}\ )\Big)\cdots \tag{4.25}$$

$$-T_e L_{g0}\Big(\frac{\partial \boldsymbol{A}_i}{\partial g}\Big|_{(r0,\ g0)} T_e L_{g0} \boldsymbol{A}_{j(r0,\ g0)}\Big) \tag{4.26}$$

where $(T_{g0}L_{g^{-1}})^{-1} = T_eL_{g0}$. Finally, substituting equations above to our original evaluation of the total lie bracket $[\dot{q_1}, \dot{q_2}]$ yields:

$$[\dot{q_1}, \dot{q_2}] \mid_{(\ r0,\ g0)} = \left[\begin{array}{l} \vec{\mathbf{0}} \\ \underbrace{-T_eL_{g0}\left(\frac{\partial \boldsymbol{A}_2}{\partial r_1} \mid_{(\ r0,\ g0)} - \frac{\partial \boldsymbol{A}_1}{\partial r_2} \mid_{(\ r0,\ g0)} \right)}_{\text{exterior derivative}} \\ \underbrace{\begin{array}{l} +T_eL_{g0}\left(\frac{\partial (T_{g0}L_{g0^{-1}} \cdot T_eL_g)}{\partial g} \mid_{(r0,\ \ g0)} \boldsymbol{A}_{2(r0,\ g0)} \left(T_eL_g\boldsymbol{A}_1 \mid_{r0,\ g0} \right) \right) \\ \cdots - T_eL_{g0}\left(\frac{\partial (T_{g0}L_{g0^{-1}} \cdot T_eL_g)}{\partial g} \mid_{(r0,\ \ g0)} \boldsymbol{A}_{1(r0,\ g0)} \left(T_eL_g\boldsymbol{A}_2 \mid_{r0,\ g0} \right) \right) \end{array}}_{\text{local lie bracket}} \\ \underbrace{\begin{array}{l} + T_eL_{g0}\left(\frac{\partial \boldsymbol{A}_2}{\partial g} \mid_{(r0,\ g0)} T_eL_g\boldsymbol{A}_1 \mid_{r0,\ g0} \right) \\ \cdots - T_eL_{g0}\left(\frac{\partial \boldsymbol{A}_1}{\partial g} \mid_{(r0,\ g0)} T_eL_g\boldsymbol{A}_2 \mid_{r0,\ g0} \right) \end{array}}_{\text{the rotational asymmetry term}} \end{array} \right] \tag{4.27}$$

The total Lie bracket is evaluated at the initial configuration of the system $q_0 = (r_0,\ g_0)$. Taking $g_0 = e$ (setting the origin of the position space at this initial configuration) effectively eliminates the T_eL_{g0} factor, and so Eqn[4.2.1] gives the average body velocity, and the integration of the corresponding total lie bracket becomes the corrected body velocity integral ($cBVI$). With properly chosen coordinates, $cBVI$ can approximate the true net displacement with minimal error.

However, replacing the initial configuration with the system identity configuration presents one complication. For gaits that start at non-identity configuration, the local connection A_b will be different with respect to system starting orientation ϕ_o. To make sure the correct A_b is calculated correctly, we introduce a new variable ω to track the amount of rotation between the system initial configuration g_0 to the system identity configuration e. Correspondingly, Eqn[4.2.1] can be represented as:

$$[\dot{q_1}, \dot{q_2}] \Big|_{r0,\ g0=e} = \left[\begin{array}{c} \vec{\mathbf{0}} \\ \underbrace{-\left(\frac{\partial \boldsymbol{A}_2}{\partial r_1} \Big|_{(r0,\ \ \omega)} - \frac{\partial \boldsymbol{A}_1}{\partial r_2} \Big|_{(r0,\ \ \omega)} \right)}_{\text{exterior derivative}} \\ \underbrace{\begin{array}{l} + \left(\frac{\partial (T_e L_g)}{\partial g} \Big|_{(r0,\ g0)} \boldsymbol{A}_{2(r0,\ \ \omega)} \left(\boldsymbol{A}_1 \Big|_{(r0,\ \ \omega)} \right) \right) \cdots \\ - \left(\frac{\partial (T_e L_g)}{\partial g} \Big|_{(r0,\ g0)} \boldsymbol{A}_{1(r0,\ \ \omega)} \left(\boldsymbol{A}_2 \Big|_{(r0,\ \ \omega)} \right) \right) \end{array}}_{\text{local lie bracket}} \\ \underbrace{\begin{array}{l} + \left(\frac{\partial \boldsymbol{A}_2}{\partial g} \Big|_{(r0,\ \omega)} \boldsymbol{A}_1 \Big|_{(r0,\ \omega)} \right) \cdots \\ - \left(\frac{\partial \boldsymbol{A}_1}{\partial g} \Big|_{(r0,\ \ \omega)} \boldsymbol{A}_2 \Big|_{(r0,\ \omega)} \right) \end{array}}_{\text{the rotational asymmetry term}} \end{array} \right] \tag{4.28}$$

The combinatory effect of the exterior derivative ($-d\boldsymbol{A}$), local lie bracket $[\boldsymbol{A}_1,\ \boldsymbol{A}_2]$ and the rotational asymmetry term gives $D(-\boldsymbol{A})$. Therefore, $D(-\boldsymbol{A})$ gains another mathematical meaning as the local curvature of the connection $r0$, evaluated at system identity configuration.

$$D(-\boldsymbol{A}) = -d\boldsymbol{A} \ + \ [\boldsymbol{A}_1,\ \boldsymbol{A}_2] \ + \ \text{the rotational asymmetry term} \tag{4.29}$$

In essence, the exterior derivative represents how the system dynamics change with the shape, and local Lie bracket and the rotational asymmetry term together represent how the system dynamics change with motion through the position space.

The effects of the exterior derivative and local lie bracket have been carefully reviewed in [12] for kinematic snake in $SE(2)$ and are not repeated here. it is importan to notice that there exist underlying parallelism between the local Lie bracket and the rotational asymmetry term. Whereas the local Lie bracket fixes the effect of local connection A_b and explains the Lie bracket non-commutativity induced by T_eL_g (the amount of rotation between the world frame and system body frame), the rotational asymmetry term fixes the effect of T_eL_g and explains the Lie bracket non-commutativity induced by the different values of A_b at different position g.

To summarize, the rotational asymmetry term measures the rates of change of $A_b\dot{r_1} = A_b^1$ and $A_b\dot{r_2} = A_b^2$ with respect to each other at different points in position space G. Flowing infinitesimally along the lie bracket formed by the rotational

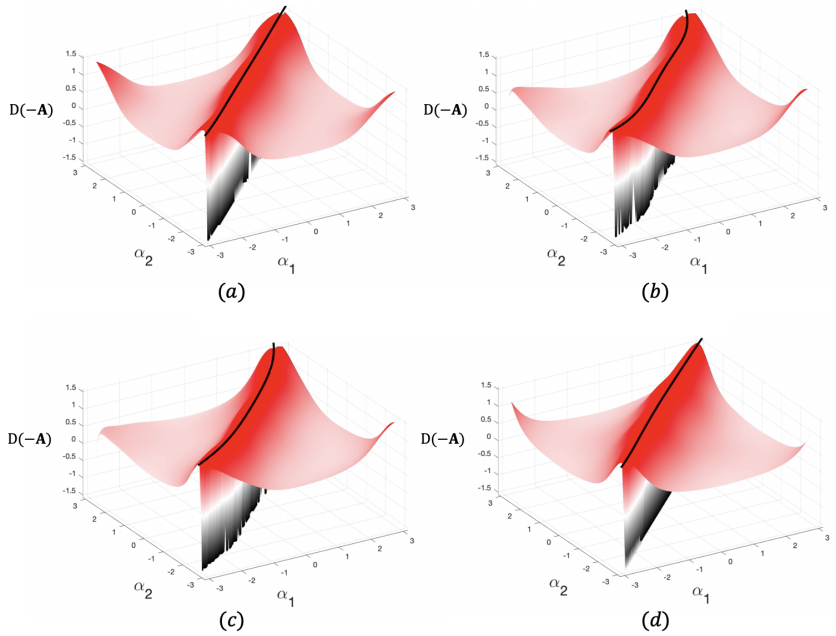

Figure 4.7: The change in the local curvature $D(-\boldsymbol{A})$, now composed of three components, with respect to system initial orientation ϕ_0. a) $\phi_0 = -\pi/2$; b) $\phi_0 = -\pi/3$; a) $\phi_0 = -\pi/4$; a) $\phi_0 = 0$. For easier visualization, the values are applied through the atan function are between $[-\pi/2, \pi/2]$. The shape space singularity line is overlaid on top of the surface plot to indicate the surface plot change.

asymmetry term is equivalent to flowing infinitesimally along A_b^1, A_b^2 , $-A_b^1$, and $-A_b^1$ in sequence on different starting point g on G. If the A_b^1 A_b^2 are constant fields on G , which is the case for 3-link kinematic snake robot in $SE(2)$, then the rotational asymmetry term is 0 everywhere. For the system on cylinder, however, A_b^1, A_{b2} are vector fields dependent on different choice of g, and thus non-zero.

.

4.3 Section Summary

Through the derivation of the reconstruction equation and the total Lie bracket, we examined how position space curvature affects the motion of a kinematic system on cylindrical surface, specifically through the derivation of local connection and the constrained curvature function. We showed that the position space curvature induces a change of the local connection co-vector fields with respect to the system

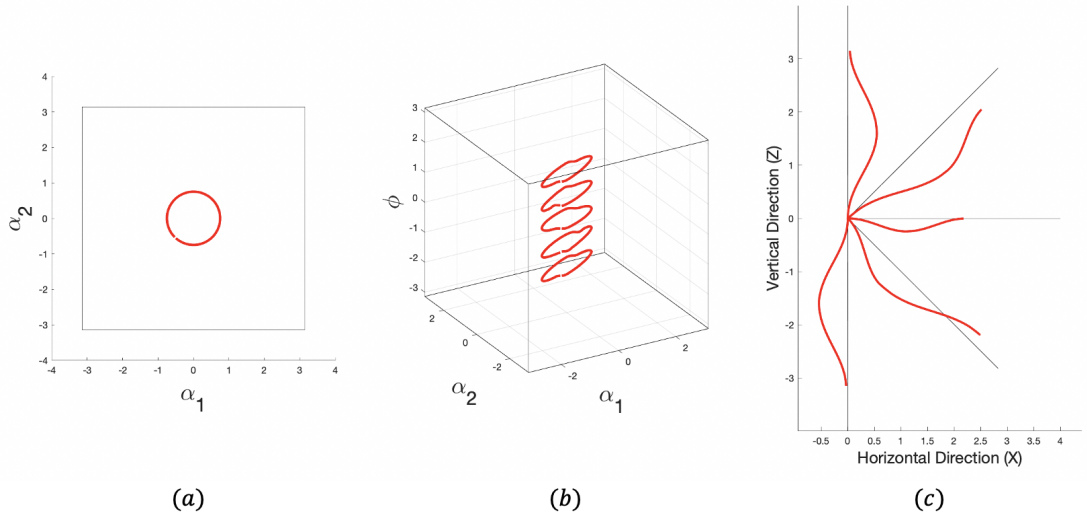

Figure 4.8: This figure shows the effect of initial orientation ϕ_0 of the system on cylinder on the position space motion. a) the five shape space trajectories (gaits) have the same circular profile when projected in α_1, α_2 plane. b)three-dimensional visualization of the the shape space trajectories, starting at $\phi_0 = [-\pi/2, -\pi/4, 0, \pi/4, \pi/2]$. c) position space trajectories of each of the five gaits, indicated with their respective orientation. Depending on ϕ_0, the net displacement and rotation of those gaits are different.

body frame orientation, which then propagates through Lie bracket averaging. As a result, we recovered an additional term that appears in the total Lie bracket of the system, which encodes information of the position space curvature.

In addition to the classical geometric analysis, we proposed a gait design scheme utilizing the gradient-descent optimizer to find the optimally efficient gait. Although we do not provide gait optimization results in this thesis, future work has already been planned to detail the optimization process.

As an example of symmetry-breaking systems whose nonholonomic constraints are dependent on coordinate choice, the studied system on cylinder sheds new light on motion planning for systems on a more diverse set of surfaces. Specifically, surfaces that exhibits features periodicity (i.e. surfaces composed of sinusoidal functions) are of high interest as the cyclical surface pattern can be leveraged in open-loop gait design.

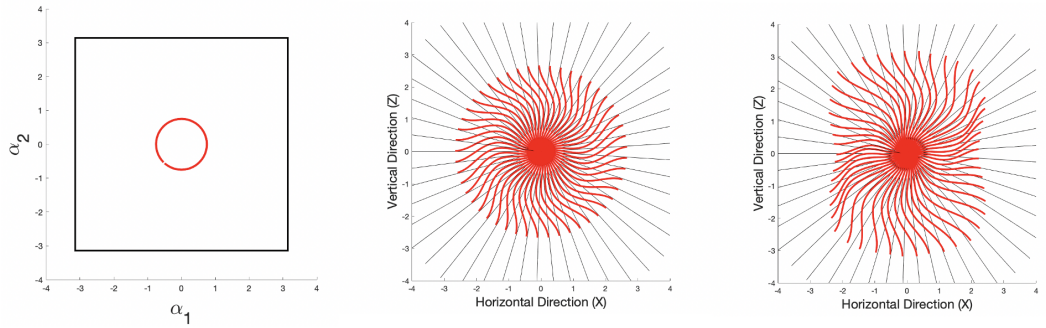

(a) (b) (c)

Figure 4.9: The comparison between how initial orientation of the system affect position space locomotion in b) kinematic snake in $SE(2)$ and c) system on cylinder. The red solid lines show the position space trajectories of the respective systems in different initial orientation. All resulting trajectories are from the same gait shown in a).

Chapter 5

Conclusion and Future Work

In this thesis, we explored geometric motion planning for two types of three-link, nonholonomic kinematic snake systems: one moves in $SE(2)$, the other on the surface of a cylinder. Although these two systems are connected by their similar geometric properties, in this work we emphasized different elements of their respective gait design strategies. In the first part, we looked at the singularity problem in 2D kinematic snake, which long poses challenge to empirical gait selection methods. At singular configurations, the locomotion system instantaneously loses one degree of control freedom, thereby making the kinematic local connection invalid. However, we identified the allowable shape space motion that respects the nonholonomic constraint and incorporated it into a "right angle crossing" curvature constraint. Furthermore, in combination with the developed gradient-descent gait optimizer, we captured the effect of singularity on system locomotion through a reverse application of Stokes' theorem, and we generated optimally gait under the efficiency metric. In the second part, we investigated how curvature in the position space of the system affects system locomotion. We analyzed how information on surface curvature manifests through a dependency on body coordinate orientation by deriving the reconstruction equation and the total Lie brackets of this newly designed system on cylinder. Because the system on cylinder is a symmetry-breaking model, geometric gait design tools that rely on invariance in system dynamics and constraint start to break down. For this reason, we proposed a corresponding gait optimization strategy utilizing the aforementioned gradient-descent optimizer that has potential of automatically generating high-efficient gaits.

Looking forward to the immediate next step, we expect to bring geometric concepts of the two systems together in closer inspection. In fact, by choosing a cylindrical surface with zero curvature, the system on cylinder effectively the

kinematic snake robot in $SE(2)$. Studying the gradual transition between the two system can potentially reveal different aspects of the position space curvature that can be utilized or ignored for efficient gait design.

In the future, we are interested in expanding our geometric analysis of system locomotion on curved position space to cover a wider range of non-flat surfaces. In particular, there are two interesting directions we want to pursue. First of all, the system on cylinder is a rather simple model, and we can potentially generalized our discovery to other link-like systems, such as low Reynolds and high Reynolds swimmers. Furthermore, at this stage we only studied contact surfaces that manifests constant curvature in a single direction. Investigating the effect of more complex surface curvatures (e.g. curved surfaces represented by combination of sinusoidal waves) may lead to exciting engineering applications that produces efficient robot gaits on truly uneven terrain. Last but not least, we hope to search for a unifying framework that systematically summarizes locomotion strategies for the symmetry-breaking systems. Such framework should ideally explains symmetry breaking phenomenon induced not only by position space curvature but also by non-conservative external actuation, such as directional force acting on the system.

Appendix A

Appendix

A.1 Pathlength Cost Metric

A differential arclength ds traveld by the system in Euclidean space is usually represent as:

$$ds = \sqrt{dx^2 + dy^2}$$

As in [8], ds is the line element of unit infinitesimal length element by the differential geometry community. Its square is the first fundamental form of the space can represented quadratically in Euclidean space as:

$$ds^2 = \begin{bmatrix} dx & dy \end{bmatrix} \underbrace{\begin{bmatrix} 1 & 0 \\ 0 & 1 \end{bmatrix}}_{\mathcal{M}} \begin{bmatrix} dx \\ dy \end{bmatrix} \tag{A.1}$$

where $\mathcal{M}$ is the Riemmanian metric tensor. When examining distances on the shape space of the three-link kinematic system, an identity metric tensor only considers joint motion, not the effort to produce the motion. It is therefore beneficial to define specific distance metrics $\mathcal{M}$ specific to measure such effort.

Since the kinematic snake models considered in this thesis accumulate and release their kinetic energy through the system action, we explore the connection between the kinetic energy KE and shape space path-length starting from the equation

$$\mathrm{KE}_i = \frac{1}{2} \xi_i^T m_i \xi_i$$

Each link i is modeled as an elongated ellipse with unit density. Therefore:

$$m_i = \begin{bmatrix} \pi ab & 0 & 0 \\ 0 & \pi ab & 0 \\ 0 & 0 & \pi ab \cdot \frac{a^2+b^2}{4} \end{bmatrix}$$

The mass matrix acts as a quadratic map from body velocity of a link to the kinetic energy required to maintain that velocity. To isolate the effect of shape space velocity to the system energy, we can pull the mass matrix M_i of the configuration space back to an effective mass matrix for that link on the shape space by pre-multiplying and post-multiplying a set of link jacobians J_i. Those jacobians maps from joint velocities $\dot{\alpha}$ to body velocities of the links.

$$\mathrm{KE}_i = \frac{1}{2}\dot{r}\left(J_i^T m_i J_i\right)\dot{r}$$

The total kinetic energy of the system is the sum of the kinetic energies associated with each individual link:

$$\mathrm{KE}sys = \sum_i \mathrm{KE}_i = \frac{1}{2}\dot{r}^T \overbrace{\left(\sum_i J_i^T m_i J_i\right)}^{\mathcal{M}} \dot{r} \tag{A.2}$$

Notice that Eqn[A.2] above bears resemblance to Eqn[A.1].

$$ds_p^2 = \mathrm{KE}_p dt^2 = dr^T \mathcal{M} dr$$

$$ds_p = \sqrt{\mathrm{KE}}\; dt$$

where $\mathrm{KE}_p = \dot{r_p}^T \mathcal{M} r_p$ is scaled kinetic energy of the system at a certain way point p.

Eqn[A.2] has an unusual form of square-root of kinetic energy multiplied by time, but it does offer physical intuition. Reaching points further away in fixed time span requires moving at increased speed, and Eqn[A.2] ensures that the energy is proportional to velocity squared. In this sense, the metric tensor $\mathcal{M}$ can be viewed as a Riemannian metric on the joint space that encodes the effort for the kinematic snake to move through space.

Notice that in the equations above are composed differently than that of previous work [6] for low Reynolds number swimmer. Whereas the metric tensor $\mathcal{M}$ for low Reynolds swimmer maps shape velocity to power dissipation into surrounding medium, the metric tensor used here maps shape velocity to system kinetic energy.

Therefore, the weighted path-length under this metric describes the square root of energy required to execute it in unit time.

A.2 Inertial Cost Metric

Inertia is the resistance of any physical object to any change in its state of motion, including changes to its speed and direction. For most of the systems with acceleration, the cost function can be defined as torque squared, that usually takes the physical meaning as the system energy cost. For nonholomic kinematic snake driven by rotational joints, energy is spent by the joint motors to propel the system forward. Since Ohm's power law equation states:

$$P = I^2 R \tag{A.3}$$

The wattage power is thus proportion to the current squared. Moreover, because the output torque of a DC motor is directly proportional to the current through the windings:

$$\tau \propto I \tag{A.4}$$

we can combine the relationship above to define our cost of motion to be proportional the square of torque acting on the joints.

$$cost = \|\tau\|^2, \tag{A.5}$$

where τ is the torques on joints and can be found from system dynamic equation,

$$\tau = M\ddot{q} + C\dot{q}(\dot{q}, q), \tag{A.6}$$

where q is the generalized coordinates, and C is the centrifugal and Coriolis matrix. Assuming the system does not store potential energy and is isolated from external forces, the Lagrangian of the system can be reduce to purely kinetic. The inertial cost of motion is thus based on the kinetic energy needed for a given gait to be execute in unit time. The kinetic energy as a function of shape variable and their velocities can be written as:

$$T(r, \dot{r}) = KE_{sys} = \frac{1}{2}\dot{r}^T \mathcal{M} \dot{r}$$

where $\mathcal{M}$ is the 2×2 "pulled back" mass metric that captures the accumulative effect of the system's masses. The "pull back" mass matrix gives us an easier way to apply the Euler-Langrange method to the system, where the torques τ felt at

all the joints becomes:

$$\tau \;=\; \frac{d}{dt}\left(\frac{\partial T(r,\dot{r})}{\partial \dot{r}}\right) - \frac{\partial T(r,\dot{r})}{\partial r}$$

and $r = [\alpha_1,\ \alpha_2]^T$ for the kinematic snake

We can re-write the Euler-Lagrange equation above with global equations of motion abstracted:

$$\tau = \mathcal{M}_r(r)\ddot{r} + C_r(\dot{r},\ r)$$

where the matrix $C_r(\dot{r},\ r)$, which represent the Coriolis and centrifugal forces induced by instant joint movement, is given by:

$$C_r(\dot{r},\ r) = \frac{1}{2}\left(\dot{r}^T\left(\frac{\partial \mathcal{M}_r(r)}{\partial \dot{r}}\right)\dot{r} - \left(\dot{r}^T\frac{\partial \mathcal{M}_r(r)}{\partial r}\dot{r}\right)\right)$$

Details derivation is provided in details in [9].

A.3 The Geometry of System on Cylinder

The system on cylinder is a unique kinematic system. Its motion on a cylindrical surface is in 3D and thus seemingly require 6 DOF to describe, but its mechanical constraints reduce the degrees of freedom down to the three (i.e. $\theta,\ z,\ \phi$ in the system position space). Despite the simplification, it is still useful to use both the 3D coordinates and the reduced position space to describe the system position and orientation, Recognizing the various relationship these two system position space parametrization leads us into deeper understanding of how curvature of the cylinder surfaces affects the mechanical constraints, and eventually the system locomotion.

In this section, we use trigonometry to solve for the relationships between some key variables used in our work. Specifically, we show the derivation of the link wise position space variables $\theta_i,\ z_i$ and ϕ_i, and an intermediate, 3D orientation variable, ψ_i

A.3.1 Calculation of ψ_i

In three dimensional space, any 3D vector forms an angle between itself and an arbitrarily defined ground plane. Using the cylinder cross-sectional plane as the groudn plane, $\psi_i \in [0,\ \pi/2]$ describe the angle between link i and the cross-sectional plane of the cylinder. Given the system orientation ϕ_o as well as the control and

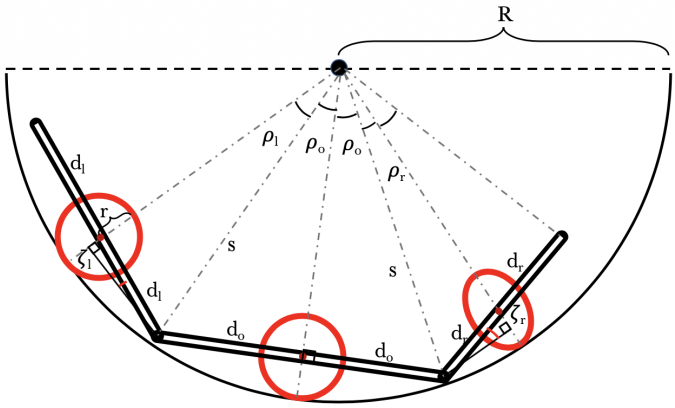

Figure A.1: Variables needed for calculating the geometric relationship between link orientation and the yaw, pitch roll angles via trigonometry

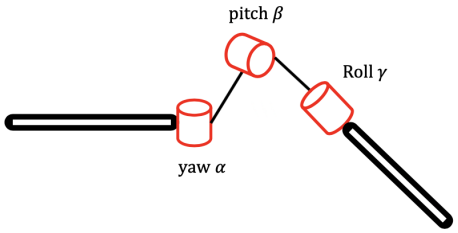

Figure A.2: Simple sketch showing one of the feasible mechanical design for the 3D joint, composed of three one-dimensional rotational joint controlling yaw(α), pitch(β), roll(γ) individually

compliant angles $\alpha,\ \beta,\ \psi_i$ can calculated by finding the orientation vector of link i using transformations in $SO(3)$, where the final rotation matrix is calculated as:

$$R_{rot} = \underbrace{\begin{bmatrix} \cos\phi_o & -sin\phi_o & 0 \\ 0 & 0 & -1 \\ \sin\phi_o & \cos\phi_o & 0 \end{bmatrix}}_{world\ to\ local\ axes\ rotation} \underbrace{\begin{bmatrix} \cos\alpha & -\sin\alpha & 0 \\ \sin\alpha & \cos\alpha & 0 \\ 0 & 0 & 1 \end{bmatrix}}_{Rotation\ around\ local\ z\ axis} \underbrace{\begin{bmatrix} \cos\beta & 0 & \sin\beta \\ 0 & 1 & 0 \\ -\sin\beta & 0 & \cos\beta \end{bmatrix}}_{Rotation\ aroudn\ local\ y\ axis}$$

Since we initial position of the middle link, before rotating $\phi_o, \alpha,\ \beta$ around their respective axes, is defined to be parallel to the ground, the Orientation vector L_i

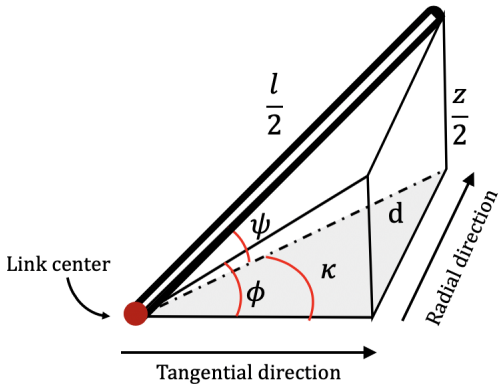

Figure A.3: Intermediate variables need to calculate projection of link i from $SE(3)$ to the local tangent plane defined the ith wheel-cylinder contact point

in 3D is thus

$$L_i = R_{rot} \cdot \begin{bmatrix} 1 \\ 0 \\ 0 \end{bmatrix} \tag{A.7}$$

$$\psi_i = \cos^{-1}\left(\frac{L_i \cdot L_{iXY\ proj}}{||L_i|| \cdot ||L_{iXY\ proj}||}\right)$$

where in eqn(?), $L_{iXY\ proj}$ is the projection of L_i on to the cylinder cross sectional plane.

A.3.2 Calculation of θ_i

For system on cylinder with wheel radius r and cylinder radius R, define intermediate variable q such that

$$q = R - r$$

We can then work out the analytical expression of ϕ_l (corresponding to the left link) using trigonometry:

$$d_l = \frac{l}{2}\cos\psi_l$$

$$s = \sqrt{d_o^2 + q^2} = \sqrt{\left(\frac{l}{2}\cos\psi_o\right)^2 + q^2}$$

Therefore, ρ_o and ρ_l, shown in Fig(?), can be calculated as:

$$\rho_o = \cos^{-1}\left(\frac{s^2+q^2-d_o^2}{2sq}\right) = \cos^{-1}\left(\frac{q}{\sqrt{\left(\frac{l}{2}\cos\psi_o\right)^2+q^2}}\right)$$

And

$$\rho_l = \cos^{-1}\left(\frac{s^2+q^2-d_l^2}{2sq}\right) = \cos^{-1}\left(\frac{2q^2+\left(\frac{l}{2}\cos\psi_o\right)^2-\left(\frac{l}{2}\cdot\cos\psi_l\right)^2}{2q\sqrt{\left(\frac{l}{2}\cos\psi_o\right)^2+q^2}}\right)$$

Notice that the relationship $\theta_l = \theta_o - \rho_0 - \rho_l$, the left link orientation, projected onto the local tangent plane, can be calculated as:

$$\theta_l = \theta_o - \cos^{-1}\left(\frac{q}{\sqrt{\left(\frac{l}{2}\cos\psi_o\right)^2+q^2}}\right) - \cos^{-1}\left(\frac{2q^2+\left(\frac{l}{2}\cos\psi_o\right)^2-\left(\frac{l}{2}\cos\psi_l\right)^2}{2q\sqrt{\left(\frac{l}{2}\cos\psi_o\right)^2+q^2}}\right) \quad \text{(A.8)}$$

Similarly, we have $\theta_r = \theta_o + \rho_0 + \rho_l$, which can be eventually written as:

$$\theta_r = \theta_o + \cos^{-1}\left(\frac{q}{\sqrt{\left(\frac{l}{2}\cos\psi_o\right)^2+q^2}}\right) + \cos^{-1}\left(\frac{2q^2+\left(\frac{l}{2}\cos\psi_o\right)^2-\left(\frac{l}{2}\cos\psi_r\right)^2}{2q\sqrt{\left(\frac{l}{2}\cos\psi_o\right)^2+q^2}}\right) \quad \text{(A.9)}$$

Eqn() and () uses arc-cosine functions and thus are correct up to the positive minus sign. Correct sign can be by inferred by neighboring values.

A.3.3 Calculation of ϕ_i

Moreover, θ_i is the projected vector of the corresponding ψ_i onto the local tangent plane, which can be found be first determining ϕ_i. The relationship between ϕ_i and ψ_i can be captured in the following steps

let variable u_i be the tangent vector at the wheel-cylinder contact point.

$$u_i = \begin{bmatrix} \sin\theta_i \\ -\cos\theta_i \\ 0 \end{bmatrix}$$

Project the 3D link orientation vector L_i onto the local tangent plane gives

$$L_{it\ proj} = L_i - \frac{L_i \cdot u_i}{||u_i||^2} \cdot u_i$$

Where $L_{it\ proj}$ is a 3×1 vector denoting the projected vector in 3D.

Within local tangent plane, $L_{it\ proj}$ can be separated into two components, the first one tangent to the curvature of the cylinder, and the second one orthogonal to the first one. We use variables $e_{t\parallel}$ and $e_{t\perp}$ to represent the two components on the local tangent plane. Therefore:

$$e_{t\perp} = L_{T\ proj}(z)$$

$$e_{t\parallel} = sign\left(\frac{L_{it\ proj} \cdot u_i}{||L_{it\ proj}|| \cdot ||u_i||}\right) \cdot (L_{it\ proj}(x) + L_{it\ proj}(y))^2$$

and so the link-wise orientation in the local tangent plane is

$$\phi_i = tan_2^{-1}\left(\frac{e_{t\perp}}{e_{t\parallel}}\right)$$

A.4 Average Body Frame for System on Cylinder

We started with the kinematic snake constraint equation:

$$\overbrace{\begin{bmatrix} -\sin\phi_l & \cos\phi_l & -\sin\phi_l \cdot \frac{\partial x_l}{\partial \phi_o} + \cos\phi_l \cdot \frac{\partial z_l}{\partial \phi_o} \\ -\sin\phi_o & \cos\phi_o & 0 \\ -\sin\phi_r & \cos\phi_r & -\sin\phi_r \cdot \frac{\partial x_r}{\partial \phi_o} + \cos\phi_r \cdot \frac{\partial z_r}{\partial \phi_o} \end{bmatrix}}^{\omega(\xi)} \begin{bmatrix} \dot{x_o} \\ \dot{z_o} \\ \dot{\phi_o} \end{bmatrix} + \ldots$$
$$\overbrace{\begin{bmatrix} -\sin\phi_l \cdot \frac{\partial x_l}{\partial \alpha_l} + \cos\phi_l \cdot \frac{\partial z_l}{\partial \alpha_l} & 0 \\ 0 & 0 \\ 0 & -\sin\phi_r \cdot \frac{\partial x_r}{\partial \alpha_r} + \cos\phi_r \cdot \frac{\partial z_r}{\partial \alpha_r} \end{bmatrix}}^{\omega(r)} \begin{bmatrix} \dot{\alpha_l} \\ \dot{\alpha_r} \end{bmatrix} = \begin{bmatrix} 0 \\ 0 \\ 0 \end{bmatrix} \tag{A.10}$$

Lets re-write to:

$$\begin{bmatrix} w_{11} & w_{12} & w_{13} & w_{14} & w_{15} \\ w_{21} & w_{22} & w_{23} & w_{24} & w_{25} \\ w_{31} & w_{32} & w_{33} & w_{34} & w_{35} \end{bmatrix} \begin{bmatrix} \dot{x_o} \\ \dot{z_o} \\ \dot{\phi_o} \\ \dot{\alpha_1} \\ \dot{\alpha_2} \end{bmatrix} = \vec{\mathbf{0}}$$

Using the average orientation frame, we fixed the origin of the body frame as it is (at the center of the mid link), but rotate the frame such that the new orienation of the body frame represents the average orientation of the 3 links.

Thus,

$$\dot{\phi}_{ave} = \frac{\dot{\phi}_l + \dot{\phi}_0 + \dot{\phi}_r}{3} = \frac{\left(\dot{\phi}_0 - \dot{\alpha}_1\right) + \dot{\phi}_0 + \left(\dot{\phi}_0 + \dot{\alpha}_2\right)}{3} = \dot{\phi}_0 + \frac{\dot{\alpha}_2 - \dot{\alpha}_1}{3}$$

Therefore,

$$\dot{\phi}_0 = \dot{\phi}_{ave} - \frac{\dot{\alpha}_2}{3} + \frac{\dot{\alpha}_1}{3}$$

So if we re-arrange the linear equation of the constraints, we will get:

$$\begin{bmatrix} w_{11} & w_{12} & w_{13} & w_{14} & w_{15} \\ w_{21} & w_{22} & w_{23} & w_{24} & w_{25} \\ w_{31} & w_{32} & w_{33} & w_{34} & w_{35} \end{bmatrix} \begin{bmatrix} \dot{x}_0 \\ \dot{z}_0 \\ \dot{\phi}_{ave} - \frac{\dot{\alpha}_2}{3} + \frac{\dot{\alpha}_1}{3} \\ \dot{\alpha}_1 \\ \dot{\alpha}_2 \end{bmatrix}$$

$$= \begin{bmatrix} w_{11} & w_{12} & w_{13} & w_{14} + \frac{w_{13}}{3} & w_{15} - \frac{w_{13}}{3} \\ w_{21} & w_{22} & w_{23} & w_{24} + \frac{w_{23}}{3} & w_{25} - \frac{w_{23}}{3} \\ w_{31} & w_{32} & w_{33} & w_{34} + \frac{w_{33}}{3} & w_{35} - \frac{w_{33}}{3} \end{bmatrix} \begin{bmatrix} \dot{x}_0 \\ \dot{z}_0 \\ \dot{\phi}_{ave} \\ \dot{\alpha}_1 \\ \dot{\alpha}_2 \end{bmatrix}$$

This will be our new constraint matrix, with average orientation. We can seperate the 3×5 matrix again into 2 parts again, yielding:

$$\overbrace{\begin{bmatrix} -\sin\theta_l & \cos\theta_l & -\sin\theta_l \cdot \frac{\partial \phi_l}{\partial \theta_o} + \cos\theta_l \cdot \frac{\partial y_l}{\partial \theta_o} \\ -\sin\theta_o & \cos\theta_o & 0 \\ -\sin\theta_r & \cos\theta_r & -\sin\theta_r \cdot \frac{\partial \phi_r}{\partial \theta_o} + \cos\theta_r \cdot \frac{\partial y_r}{\partial \theta_o} \end{bmatrix}}^{W(\xi)} \begin{bmatrix} R\dot{\phi}_o \\ \dot{y}_o \\ \dot{\theta}_o \end{bmatrix}$$

$$\ldots + \overbrace{\begin{bmatrix} \left(-\sin\theta_l \cdot \frac{\partial \phi_l}{\partial \alpha_l} + \cos\theta_l \cdot \frac{\partial y_l}{\partial \alpha_l}\right) + \frac{\left(-\sin\theta_l \cdot \frac{\partial \phi_l}{\partial \theta_o} + \cos\theta_l \cdot \frac{\partial y_l}{\partial \theta_o}\right)}{3} & -\frac{\left(-\sin\theta_l \cdot \frac{\partial \phi_l}{\partial \theta_o} + \cos\theta_l \cdot \frac{\partial y_l}{\partial \theta_o}\right)}{3} \\ 0 & 0 \\ \left(\frac{-\sin\theta_r \cdot \frac{\partial \phi_r}{\partial \theta_o} + \cos\theta_r \cdot \frac{\partial y_r}{\partial \theta_o}}{3}\right) & \left(-\sin\theta_r \cdot \frac{\partial \phi_r}{\partial \alpha_r} + \cos\theta_r \cdot \frac{\partial y_r}{\partial \alpha_r}\right) - \left(\frac{-\sin\theta_r \cdot \frac{\partial \phi_r}{\partial \theta_o} + \cos\theta_r \cdot \frac{\partial y_r}{\partial \theta_o}}{3}\right) \end{bmatrix}}^{W(r)} \begin{bmatrix} \dot{\alpha_l} \\ \dot{\alpha_r} \end{bmatrix} = \vec{\mathbf{0}}$$

Where $A_{avew} = -W(\xi)^{-1}W(r)$, and $A_{aveb} = T_g L_{g^{-1}} \cdot A(r)_w$ so that:

$$\begin{bmatrix} \xi_\phi \\ \xi_y \\ \xi_\theta \end{bmatrix} = A_{aveb} \begin{bmatrix} \dot{\alpha_1} \\ \dot{\alpha_2} \end{bmatrix}$$

Bibliography

[1] Gregory C Walsh and S Shankar Sastry. «On reorienting linked rigid bodies using internal motions». In: *IEEE Transactions on Robotics and Automation* 11.1 (1995), pp. 139–146 (cit. on pp. 3, 4, 22).

[2] J Ostrowski and Joel Burdick. «The mechanics and control of undulatory locomotion». In: *International Journal of Robotics Research* 17.7 (1998), pp. 683–701 (cit. on pp. 3, 4, 22).

[3] Elie A Shammas, Howie Choset, and Alfred A Rizzi. «Geometric motion planning analysis for two classes of underactuated mechanical systems». In: *The International Journal of Robotics Research* 26.10 (2007), pp. 1043–1073 (cit. on pp. 3, 4, 8).

[4] Jim Ostrowski. «Reduced equations for nonholonomic mechanical systems with dissipative forces». In: *Reports on Mathematical Physics* 42.1-2 (1998), pp. 185–209 (cit. on pp. 3, 5).

[5] Ross L Hatton and Howie Choset. «Geometric motion planning: The local connection, Stokes' theorem, and the importance of coordinate choice». In: *The International Journal of Robotics Research* 30.8 (2011), pp. 988–1014 (cit. on pp. 3, 11, 16).

[6] Suresh Ramasamy and Ross L Hatton. «The geometry of optimal gaits for drag-dominated kinematic systems». In: *IEEE Transactions on Robotics* 35.4 (2019), pp. 1014–1033 (cit. on pp. 3, 6, 42).

[7] Suresh Ramasamy and Ross L Hatton. «Soap-bubble optimization of gaits». In: *2016 IEEE 55th Conference on Decision and Control (CDC)*. IEEE. 2016, pp. 1056–1062 (cit. on pp. 3, 5, 6, 11, 12).

[8] Ross L Hatton and Howie Choset. «Kinematic cartography for locomotion at low Reynolds numbers». In: *Proc. Robot. Sci. Syst. VII* (2011) (cit. on pp. 3, 41).

[9] Hossein Faraji Ross L Hatton and Zachary Brock. «Geometric Motion Planning for Inertial Systems (in preparation)». In: (2020) (cit. on pp. 3, 6, 11, 44).

[10] Ross L Hatton and Howie Choset. «Connection vector fields for underactuated systems». In: *2008 2nd IEEE RAS & EMBS International Conference on Biomedical Robotics and Biomechatronics*. IEEE. 2008, pp. 451–456 (cit. on pp. 4, 8).

[11] James P Ostrowski, Jaydev P Desai, and Vijay Kumar. «Optimal gait selection for nonholonomic locomotion systems». In: *The International journal of robotics research* 19.3 (2000), pp. 225–237 (cit. on p. 5).

[12] Ross L Hatton and Howie Choset. «Nonconservativity and noncommutativity in locomotion». In: *The European Physical Journal Special Topics* 224.17 (2015), pp. 3141–3174 (cit. on pp. 5, 9, 12, 13, 16, 31, 35).

[13] Ross L Hatton and Howie Choset. «Geometric swimming at low and high Reynolds numbers». In: *IEEE Transactions on Robotics* 29.3 (2013), pp. 615–624 (cit. on pp. 5, 20, 22).

[14] Tony Dear, Scott David Kelly, Matthew Travers, and Howie Choset. «Locomotive analysis of a single-input three-link snake robot». In: *2016 IEEE 55th Conference on Decision and Control (CDC)*. IEEE. 2016, pp. 7542–7547 (cit. on p. 10).

[15] Tony Dear, Scott David Kelly, Matthew Travers, and Howie Choset. «The three-link nonholonomic snake as a hybrid kinodynamic system». In: *2016 American Control Conference (ACC)*. IEEE. 2016, pp. 7269–7274 (cit. on p. 10).

[16] Scott D Kelly and Richard M Murray. «Geometric phases and robotic locomotion». In: *Journal of Robotic Systems* 12.6 (1995), pp. 417–431 (cit. on p. 22).

[17] Tony Dear. «Extensions of the Principal Fiber Bundle Model for Locomoting Robots». PhD thesis. Carnegie Mellon University, 2018 (cit. on p. 22).